Air–Sea/Land Interaction in the Coastal Zone

Andrey A. Grachev • Laura S. Leo • Harindra J. S. Fernando • Christopher W. Fairall • Edward Creegan • Byron W. Blomquist • Adam J. Christman • Christopher M. Hocut

Boundary–Layer Meteorology

Manuscript submitted: 16 March, 2017
Revised: 08 November 2017

Andrey A. Grachev (✉) • Byron W. Blomquist
NOAA Earth System Research Laboratory / Cooperative Institute for Research in Environmental Sciences, University of Colorado, 325 Broadway, R/PSD3, Boulder, CO 80305-3337, USA
e-mail: Andrey.Grachev@noaa.gov

Andrey A. Grachev • Laura S. Leo • Harindra J. S. Fernando • Byron W. Blomquist • Adam J. Christman
Department of Civil & Environmental Engineering & Earth Sciences, University of Notre Dame, Notre Dame, IN, USA

Christopher W. Fairall
NOAA Earth System Research Laboratory, Boulder, CO, USA

Edward Creegan • Christopher M. Hocut
U.S. Army Research Laboratory, White Sands Missile Range NM, USA

Abstract

Atmospheric turbulence measurements made at the U.S. Army Corps of Engineers Field Research Facility (FRF) located on the Atlantic coast near the town of Duck, North Carolina during the CASPER-East Program (October–November 2015) are used to study air–sea/land coupling in the FRF coastal zone. Turbulence and mean meteorological data were collected at multiple levels (up to four) on three towers deployed at different landward distances from the shoreline, with a fourth tower located at the end of a 560-m-long FRF pier. The data enable comparison of turbulent fluxes and other statistics, as well as investigations of surface-layer scaling for different footprints, including relatively smooth sea-surface conditions and aerodynamically rough dry inland areas. Both stable and unstable stratifications were observed. The drag coefficient and diurnal variation of the sensible heat flux are found to be indicators for disparate surface footprints. The drag coefficient over the land footprint is significantly greater, by as much as an order of magnitude, compared with that over the smooth sea-surface footprint. For onshore flow, the internal boundary layer in the coastal zone was either stable or (mostly) unstable, and varied dramatically at the land-surface discontinuity. The offshore flow of generally warm air over the cooler sea surface produced a stable internal boundary layer over the ocean surface downstream from the coast. While the coastal inhomogeneities violate the assumptions underlying Monin-Obukhov similarity theory (MOST), any deviations from MOST are less profound for the scaled standard deviations and the dissipation rate over both water and land, as well as for stable and unstable conditions. Observations, however, show a poor correspondence with MOST for the flux-profile relationships. Suitably-averaged, non-dimensional profiles of wind speed and temperature vary significantly among the different flux towers and observation levels, with high data scatter. Overall, the

statistical dependence of the vertical gradients of scaled wind speed and temperature on the Monin-Obukhov stability parameter in the coastal area is weak, if not non-existent.

Keywords Air–sea/land interaction • Coastal zone • Internal boundary layer • Monin-Obukhov similarity theory

1 Introduction

Quantifying the momentum, heat and mass exchange between the atmosphere and underlying surface is a central problem of atmospheric boundary-layer (ABL) research. Parametrization of air–sea/land fluxes (i.e., flux-gradient relationships) is of obvious relevance for the modelling of coupled atmosphere–ocean/land systems, including climate modelling, weather forecasting, environmental impact studies, and many other applications, e.g., offshore wind farms, as well as predicting electromagnetic signal propagation, including the presence of electromagnetic ducting.

Traditionally, the flux-gradient and flux-variance relationships in the surface layer are described by Monin-Obukhov similarity theory, hereinafter MOST (Monin and Obukhov 1954), which assumes horizontal homogeneity of the underlying surface, including surface fluxes as well as aerodynamic and thermal roughnesses (e.g., Monin and Yaglom 1971; Stull 1988; Sorbjan 1989; Garratt 1992; Kaimal and Finnigan 1994; Wyngaard 2010). While this assumption is reasonable in many situations, and enables focusing on one-dimensional processes, it is violated in the coastal zone where the horizontal gradients are sharp. A coastal zone is the interface between water and land footprints. The ocean has a relatively smooth surface (compared with land) and a very large heat capacity, which enables heat storage for extended periods, and permits turbulent mixing to larger depths, with consequences for the diurnal cycle over water. In contrast, dry inland areas are aerodynamically rough in general and have a low heat-storage capacity, thus exhibiting a stronger diurnal cycle of the sensible heat flux. Thus, the failure of the horizontal-homogeneity assumption is obvious, and the roughness discontinuity of surface properties between the ocean and land leads to the formation of a distinct internal momentum boundary layer (IBL) for onshore and offshore flow.

While there is a long history of experimental investigation of MOST for a stationary atmospheric surface layer over horizontally-homogeneous surfaces, and the relevant literature is voluminous (see, for example, the surveys in Monin and Yaglom 1971; Högström 1988; Stull 1988; Sorbjan 1989; Garratt 1992; Kaimal and Finnigan 1994; Andreas 2002; Wyngaard 2010), considerably fewer experimental studies exist for coastal margins. In most cases, observational studies in coastal zones are associated with measurements of the turbulent transfer coefficients (drag coefficient, Stanton and Dalton numbers) and other variables over coastal waters (offshore areas), with the focus on any differences with open-ocean conditions, deviations from MOST, fetch-limited conditions, the dynamics of the surface wave field over shoaling water, etc. (e.g., Katsaros et al. 1987; Geernaert 1988; Smith et al. 1992; Mahrt 1999). A number of important results from air–sea-interaction research in coastal zones were obtained during the Risø Air Sea Experiment (RASEX) in 1994 based on the measurements made at two offshore towers and one tower on the coast on the island of Lolland, Denmark. The RASEX campaign formed one of the first large datasets of detailed information on the effects of coastal processes on momentum, mass, and heat exchange (e.g., Mahrt et al. 1996, 1998, 2001a; Vickers and Mahrt 1997, 1999).

Compared with open-ocean situations, the RASEX data represent fetch-limited conditions, with the RASEX drag coefficient reported by Mahrt et al. (1996) to be significantly larger for short fetch conditions, particularly at high wind speeds. According to Vickers and Mahrt (1997), the neutral drag coefficient observed in the RASEX data depends on the wave age, the frequency bandwidth of the wave spectra, and the wind speed. In contrast to the aerodynamic roughness length, which is dominated by the wave state, the thermal roughness length in the coastal zone shows a significant dependence on the wave state only for young seas (Mahrt et al. 1998). Additionally, the thermal roughness length observed in the RASEX data is related to the occurrence of an IBL. According to Mahrt et al. (1998), the development of thin IBLs for offshore flow substantially reduces the heat transfer and thermal roughness length, but has no obvious influence on the momentum roughness length. Based on the mid-latitude coastal-zone observations from different field campaigns, Vickers and Mahrt (2010) additionally found that the roughness lengths for momentum and sensible heat appear to be smaller than those given by the widely-used Coupled Ocean–Atmosphere Response Experiment (COARE) bulk flux algorithm (Fairall et al. 2003) in conditions of weak to moderate wind speeds.

Offshore flow is traditionally described in terms of IBL development (Garratt 1987, 1990; Garratt and Ryan 1989). For offshore flow of warm air over cooler water, the turbulence in the stable IBL is suppressed by a combination of stable stratification and reduced sea-surface roughness (Fairall et al. 2006; Mahrt et al 2016), resulting in surface fluxes substantially less than that predicted by MOST (Mahrt et al. 1998). Formation of the IBL creates a decoupled boundary-layer system, where the flow at greater heights becomes partially decoupled from the surface (Smedman et al. 1997a, b; Mahrt et al. 2001b), and may form a low-level wind-speed maximum (Smedman et al. 1995; Vickers et al. 2001).

Fairall et al. (2006) examined observations obtained in 2004 during the New England Air Quality Study (NEAQS-04) of shallow, stable boundary layers in the cool coastal waters of the Gulf of Maine, between Cape Cod and Nova Scotia. Direct comparisons of the NEAQS-04 flux observations with the COARE bulk flux algorithm (Fairall et al. 2003) shows a significant reduction of the transfer coefficients for momentum, sensible heat, and latent heat associated with lighter wind speeds, more stable surface layers, and lower IBL heights. Grachev et al. (2011) used the data collected on board the *R/V Ronald H. Brown* in 2006 during the Texas Air Quality Study (TexAQS) campaign to compare turbulent fluxes measured over different footprint surfaces, including relatively smooth water surfaces (coastal waters of the Gulf of Mexico, nearby bays and harbour areas of south-eastern Texas) and aerodynamically rough urban/suburban inland areas along ship channels and rivers (up to 12 km from downtown Houston). According to Grachev et al. (2011), the COARE bulk flux algorithm (Fairall et al. 2003) reasonably describes the air–sea turbulent fluxes measured over the coastal waters of the Gulf of Mexico, although the bulk algorithm overestimates the sensible and latent heat flux by approximately 10%. Thus, the data collected during the TexAQS 2006 field campaign show that air–sea fluxes measured over the Gulf of Mexico are less influenced by coastal effects compared with those measured over the Gulf of Maine during the NEAQS 2004 campaign (Fairall et al. 2006).

Application of the bulk aerodynamic method to spatially-averaged fluxes over heterogeneous surfaces was examined by Mahrt (1996) for a wide spectrum of horizontal spatial scales. Mahrt's (1996) interpretative literature survey is based mainly on qualitative scaling arguments and limited data, which lead to a tentative unified picture of the qualitative influence of surface heterogeneity. Geernaert (2002, 2007, 2010) proposed extending MOST to accommodate non-stationarity and spatial heterogeneity over the coastal ocean. A more general form of the flux-profile relationships has been derived for both wind speed and scalars, which takes into account the flux divergences present in inhomogeneous regions, such as coastal zones (Geernaert 2002). Using this theory, Geernaert (2007) further introduced a more general equation to predict the duct height for accommodation of weak horizontal variations of wind speed, temperature, humidity, and IBL depth, whereas Geernaert (2010) derived an extended representation of the normalized drag coefficient and normalized Stanton and Dalton numbers to account for non-stationarity and the spatial variability of bulk quantities.

Electromagnetic wave propagation near the surface is significantly affected by variations of local meteorological conditions and ABL structure, because atmospheric refractivity is directly related to basic meteorological parameters. As a radio ray bends downwards (or upwards) when the atmospheric refractivity decreases (or increases) with height, a beam bending towards the surface may become "trapped" in a shallow, near-surface layer called a duct, which is a region of negative refraction gradient (e.g., Brooks et al. 1999; Brooks 2001; Atkinson and Zhu 2005, and references therein). A duct is a waveguide that significantly enhances the range over which the electromagnetic signal can travel. The work described herein was conducted as a part of the Coupled Air–Sea Processes and Electromagnetic Ducting Research (CASPER) program, which is a five-year multi-disciplinary effort to better understand ducting in the coastal zone, and which requires understanding of flow and turbulence, as well as air–sea exchanges in the coastal marine ABL. To this end, comprehensive measurement and numerical modelling programs were conducted during October–November 2015 as a part of the CASPER-East field study, with the U.S. Army Corps of Engineers Field Research Facility (FRF) located on the Atlantic Ocean near the town of Duck, North Carolina (Alappattu et al. 2017; Wang et al. 2017) selected as the coastal anchor location.

2 The CASPER-East Observation Site and Instrumentation

The CASPER-East field program involved measurements on the coastal shelf of North Carolina using a research vessel, covering either side of the air–water interface, as well as measurements at a coastal site emphasizing spatial heterogeneities of the ABL at multiple scales. Of particular interest is the development of the IBL over inhomogeneous regions, surface wave and swell effects, and non-stationary conditions. These effects contravene the underlying assumptions of MOST, and thus the basis of coupled environmental forecast models and evaporative-duct models. The CASPER-West campaign is to be conducted in September–October 2017 off the coast of California, again concentrating on evaporative ducts in the coastal shelf, as well as IBLs in the coastal zone. General information about the CASPER program and related field experiments can be found in Alappattu et al. (2017) and Wang et al. (2017).

We present data of atmospheric turbulence collected at the FRF site located near the seaside town of Duck, North Carolina (north of Kitty Hawk, North Carolina), during the CASPER-East field campaign from 8 October through 9 November 2015. The facility situated in the Outer Banks stretches from the Atlantic Ocean to Currituck Sound (Fig. 1). The Outer Banks is a 320-km-long string of low, narrow sandy reefs (peninsulas and barrier islands) separating the Atlantic Ocean (to the east) from a system of wide, shallow sounds and the forested, low-lying mainland of North Carolina (to the west). An overview of North Carolina's coastal barrier islands, sounds, estuaries, tides, waves, storm surge and other relevant information can be found in the U.S. Geological Survey publications by Dolan and Lins (1986) and Dolan et al (2016).

The centrepiece of the FRF site is a pier (Fig. 1) whose deck is 7.7 m above the sea surface, and is designed to remain above storm waves. The pier deck is 6 m wide and extends 560 m from the dunes to a nominal water depth of approximately 7 m. The FRF pier is oriented along ≈72° (in an east-north-east–west-south-west direction) and a shoreline is aligned approximately in a north-north-west–south-south-east direction (bearing ≈−18°).

Turbulent and mean meteorological data were collected at multiple (from two to four) levels on three towers deployed on land and a fourth tower located at the end of the FRF pier, hereafter called the "Pier tower" (Fig. 1). Figure 2 shows an overall view of the three shore flux towers named "Video" (or "Tall"), "Sand Dune Top" (SDT), and "Sand Dune Foot" (SDF) towers, and located at progressive distances from the shoreline (from the beach in close proximity to the water extending to the coastal sand dunes). All towers were instrumented with fast-response three-axis R.M. Young (Model 81000) sonic anemometers which sampled the velocity and sonic temperature at 20 Hz, as well as slow-response Campbell Scientific temperature/relative humidity (T/RH) probes (Model HC2S3) and air-pressure sensors (Model CS106) sampling at 1 Hz. The Pier and the SDT towers were also instrumented with LI-COR Inc. fast-response (20 Hz) open-path infrared gas analyzers (Model LI-7500A) for direct measurements of the turbulent water vapour flux (latent heat) and other relevant turbulent statistics.

Two pre-existing FRF towers (Pier and Video) were locally available for use. The Pier tower was instrumented with three levels of sonic anemometers and three levels of the slow-response T/RH probes (see Table 1). The LI-7500A gas analyzer was mounted on the same boom as the sonic anemometer at Level 1 (Fig. 3a). An additional sonic anemometer was installed on 30 October at ≈0.2 m below the pier deck ("Level 0"). On the shore, the sonic anemometers and the slow-response T/RH probes were placed at four levels on the 43-m (120 ft.) tall FRF observation "Video" tower (Fig. 3b). The Video tower base ("ground level" for this tower) is 5 m above sea level (a.s.l.).

Additionally, two 6-m tall towers (SDT and SDF) were erected on the shore between the FRF Video tower and the sea surf line (Fig. 2). The SDT tower (Fig. 3c) was located at the top of a sand dune of elevation (with bushes) ≈2.5 to 3 m above the sea shore (Figs. 2 and 3d), giving a tower base ("ground level" for this tower) elevation of ≈7 m a.s.l. The SDT tower was instrumented with three levels of sonic anemometers, with one LI-7500A sensor mounted at Level 1, and two levels of T/RH sensors (Fig. 3c). The SDF tower (Fig. 3d) was located on the shoreline at the foot of the sand dunes in close proximity to the water, with the exact distance from the sea surf line variable depending on the flow and tidal regimes, and instrumented with two levels of sonic anemometers and two levels of T/RH sensors (see Table 1). The SDF tower base ("ground level" for this tower) is elevated to ≈5 m a.s.l. In addition to the fixed tower sites, eddy-covariance data and lidar observations were collected in the coastal zone aboard a mobile platform from the bow tower of the R/V *Atlantic Explorer* (Wang et al. 2017). Measurements of bulk and skin sea-surface temperature offshore the town of Duck made aboard R/V *Hugh R. Sharp* during CASPER-East are discussed by Alappattu et al. (2017).

The mean wind speed and wind direction are derived from the sonic-anemometer data, with the rotation of the anemometer axes in a streamline coordinate system based on 30-min-averaged 20-Hz measurements of the velocity components. We use the most common method, which is a double rotation of the anemometer coordinate system, to compute the longitudinal, lateral, and vertical velocity components in real time (Kaimal and Finnigan 1994, Sect. 6.6). The measurements of the air temperature and relative humidity at several levels provided by the T/RH probes are used to evaluate the vertical temperature and humidity gradients based on 30-min-averaged 1-Hz data. Turbulent covariance and variance values are derived from the sonic anemometer/thermometers through frequency integration of the appropriate cospectra and spectra computed from 27.31-min data blocks (corresponding to 2^{15} data points) from the original 30-min data files. The dissipation rate of turbulent kinetic energy (TKE) and destruction rate for half the temperature (humidity) variance are estimated using the standard techniques based on the assumption of an inertial subrange according to Grachev et al. (2015, 2016). Other details of the turbulent measurements, turbulent data processing, accuracy, calibration, and data-quality criteria can be found in Grachev et al. (2013, 2015, and 2016).

Note that ABL observations, including turbulence measurements in the coastal zone near Duck North Carolina, have been previously reported during the Shoaling Waves Experiment (SHOWEX) for October–November 1997, March 1999 and November–December 1999. The data collected by a Long-EZ research aircraft over Atlantic coastal waters off the Outer Banks near Duck North Carolina were analyzed by Sun et al. (2001) and Vickers et al. (2001). Mahrt et al. (2001b) compared the aircraft data with sonic-anemometer data collected from buoys and a tower at the end of the FRF pier. Moreover, Friebel et al. (2009) described long-term turbulent measurements of the drag coefficient carried out at the FRF pier in Duck North Carolina from October 2005 through December 2007. These studies contain additional information about the FRF site, as well as the ABL structure and turbulent exchange in the coastal zone near Duck.

3 Measurements over Different Surface Footprints

We present time series (Sect. 3.1) and the dependence on wind direction (Sect. 3.2) of turbulence and mean meteorological data collected at multiple levels on three towers deployed on land at progressive distances from the shoreline (from the beach in close proximity of the water to the coastal sand dunes), and the fourth tower located at the end of a 560-m-long pier described in Sect. 2.

3.1 Data: Time Series

Traditional time series provide a general overview of weather conditions, turbulent fluxes, and other relevant variables, and can provide additional useful information which cannot be generally derived from various scatter plots. Figure 4 shows the time series of 30-min-averaged basic meteorological variables observed over water at the Pier tower. Time series of wind speed and direction, air temperature, and relative humidity observed at the coastal towers are very similar to those presented in Fig. 4, and thus are not shown here. The (Atlantic) coastal zone climate is distinctly maritime, with relatively small diurnal temperature and humidity variations (Fig. 4c, d). Additionally, the coastal zone is subject to thermally-driven flows, such as sea breezes (or onshore breezes) and land breezes (or offshore breezes). The occurrence of sea–land breeze systems (thermal circulation) was observed with wind speeds typically not exceeding 4–5 ms^{-1}, e.g., for the Day-of-Year (hereafter abbreviated as DOY) 293–296.5 (Fig. 4), with onshore flow during the day (sea breeze) and offshore flow during the night (Fig. 4b). The slow variation of the wind direction with a period of about 3–4 days for the DOY 297–311 is presumably due to synoptic-scale weather patterns.

The turbulent fluxes of momentum τ (or the magnitude of the wind stress), sensible heat H_S, and latent heat H_L can be estimated by the eddy-correlation method according to

$$\tau = \tau_x \equiv \rho u_*^2 = -\rho \overline{u'w'} \, , \quad (1)$$

$$H_S = c_p \rho \overline{w'\theta'} \quad (2)$$

and

$$H_L = L_e \rho \overline{w'q'} \, , \quad (3)$$

where $u_* = \sqrt{-\overline{u'w'}}$ is the friction velocity, ρ is the mean air density, θ is the potential temperature, q is the air specific humidity, c_p is the specific heat capacity of air at constant pressure, and L_e is the latent heat of evaporation of water. Here, u and w are the longitudinal and vertical velocity components, respectively, $[\,']$ denotes fluctuations about the mean value, and the overbar is an averaging operator. In Eq. 1, $\tau_x = -\rho \overline{u'w'}$ represents the longitudinal (or downstream) component of the wind stress. Note that the traditional MOST assumes stress and velocity vectors aligned in the same direction, so that the lateral (or crosswind) stress component $\tau_y = -\rho \overline{v'w'} = 0$ by definition, where v is the lateral velocity component. Thus, u_* should be computed based on the downstream component of the wind stress τ_x only for the purposes of verification and validation of MOST (Sect. 4).

Time series of u_*, H_S, H_L defined by Eqs. 1–3, and the Monin-Obukhov stability parameter $\zeta \equiv z/L$ (Monin and Obukhov 1954) for the 30-min-averaged turbulent data collected over the water (Pier tower) and land (Video and SDT towers), are shown in Figs. 5 and 6, respectively. The Monin-Obukhov stability parameter is defined as the ratio of z to the Obukhov length scale L (Obukhov 1946),

$$\zeta = \frac{z}{L} = -\frac{z\,\kappa\,g\,\overline{w'\theta_v'}}{u_*^3\,\theta_v} , \tag{4}$$

where θ_v is the virtual potential temperature, g is the acceleration due to gravity, and κ is the von Kármán constant, which is included in the definition of L simply by convention; a value of $\kappa = 0.4$ is adopted here. Below, the Monin-Obukhov stability parameter, the friction velocity u_*, and the temperature scale θ_* (defined shortly) are estimated based on the turbulent fluxes measured at each observational level (local scaling).

According to data shown in Fig. 5, the temporal patterns of the turbulent fluxes and ζ at each site are similar to one another, while also linked to the wind speed plotted in Fig. 4a. Periods of stable and unstable stratification are both observed over the water (Fig. 5g) and over the land (Fig. 5h). The traditional sign convention for the Monin-Obukhov stability parameter is used, where $\zeta > 0$ corresponds to a stable boundary layer (SBL), and $\zeta < 0$ represents a convective boundary layer (CBL). Although the temporal development of various turbulent fluxes in Fig. 5 are very similar at both the Pier and Video towers, there are noticeable differences between these two locations associated with the different aerodynamic and thermal properties of the underlying surfaces. According to Figs. 5a and 5b, the amplitude of the 30-min-averaged values of the friction velocity observed at the Pier tower is generally less than that at the Video tower, which may be attributed to the relatively smoother water surface compared with that of land.

Additionally, values of both latent and sensible heat flux display marked differences when measured over water (Fig. 5c, e) as compared with over land (Fig. 5d, f). The average latent heat flux H_L observed over land at the SDT tower (Fig. 5f) is somewhat lower than H_L measured over water at the Pier tower (Fig. 5c). Furthermore, the pronounced diurnal cycle evident in the sensible heat flux H_S observed at the Video tower (Fig. 5h) is less conspicuous at the Pier tower, which can be attributed to the different specific heat capacities between water and land as discussed in Sect. 1.

3.2 Data: Dependence on Wind Direction

The complexity of the coastal environment of the Outer Banks near Duck, North Carolina (Fig. 1) makes interpretation of the coastal ABL data difficult. The surface heterogeneity produces a complex vertical structure, including the formation of IBLs and roughness sublayers where turbulence parameters become functions of the wind direction and, therefore, surface footprints (cf. Klipp 2007). Here, the drag coefficient and the sensible heat flux in the coastal zone are examined as a function of the wind direction (Fig. 6). Recall that the pier is oriented ≈72° from north (see the solid vertical lines in Fig. 6), perpendicular to the shoreline. Thus, onshore wind directions range from 342° through 162° clockwise (see the dash-dot vertical lines in Fig. 6). Based on the data collected at the FRF pier over a twenty-seven month period between October 2005 through December 2007 (18,927 30-min data points), Friebel et al. (2009) reported that, during this period, the prevailing wind direction at Duck North Carolina is from the north-east (Ibid., Fig. 4) due to typical storms that frequent the eastern seaboard.

Figure 6 shows the drag coefficient C_D as a function of the true wind direction at all tower locations. The drag coefficient is defined as

$$C_D = \tau / \rho U^2 = \left(u_* / U\right)^2 \ , \tag{5}$$

where the momentum flux τ is based on the longitudinal wind-stress component (see Eq. 1), and U is the mean wind speed at the measurement height z derived from a sonic anemometer (for further details regarding C_D and an aerodynamic roughness length z_0 closely related to C_D, see, e.g., Grachev et al. 1998; 2011). According to Fig. 6, the drag coefficient is very sensitive to the change in wind direction, which results in the sampling of very different upwind surface characteristics. As might be expected, the observed drag coefficient over a rough land surface differs widely from that over the sea surface. Of all of the towers, the Pier tower instrumentation captures relatively low values of C_D (Fig. 7a) for all directions, except during offshore flow (wind directions between 210° and 320°), while for onshore flow, $C_D \approx 1.0 \times 10^{-3}$–$1.3 \times 10^{-3}$, suggesting close agreement between measured air–sea fluxes and estimates based on the COARE bulk flux algorithm for open-ocean conditions (Fairall et al. 2003, Figs. 2, 5, 10).

The interpretation of atmospheric turbulence measurements largely depends on the upwind 'flux footprint' over which the turbulent fluxes and other statistics are sampled. Generally, the flux footprint is a surface area at some distance along the upwind fetch contributing to the effective sources and sinks of a measured signal (Burba 2013; Leclerc and Foken 2014; and references therein). Existing footprint models (e.g., Horst and Weil 1992, 1994; Kormann and Meixner 2001; Kljun et al. 2004, 2015; Klaassen and Sogachev 2006; Wilson 2015; Glazunov et al. 2016) seek to describe the spatial extent and position of the surface area contributing to a sampled turbulent flux, depending on the measurement height, upwind and crosswind distance, thermal stratification, and surface roughness. Thus, in the case of an inhomogeneous surface, such as a coastal zone, instruments mounted at different levels on the same tower may have very different flux footprints corresponding to either a relatively smooth sea surface or aerodynamically rough dry inland areas. This sharp change in the surface characteristics due to the sea–land transition leads to the formation of a thin IBL resolved by the tower. As mentioned above, according to CASPER-East observations, the drag coefficient and diurnal variation of the sensible heat flux can be considered as indicators for different types of surface footprints.

The average C_D values over land footprints can be an order of magnitude larger than over the sea surface due to the change in aerodynamic properties of the surface. The SDT and Video tower data show elevated C_D values for offshore wind directions between ≈150° and 250° (Fig. 6e, g). Our results in Fig. 6 are mostly in reasonable qualitative agreement with our previously reported values of C_D over land/sea areas (e.g., Grachev et al. 2011, and references therein). Moreover, the drag coefficient also increases dramatically where a nearby obstruction is immediately upwind of a sonic anemometer, or when an instrument is within a deep roughness sublayer. At the SDT tower (Fig. 6e), the largest C_D values are associated with the sonic anemometer at level 1 and correspond to upwind locations of the pier deck. The pier deck is 7.7 m a.s.l. and the sonic anemometer, which is mounted approximately at the same level (7.04 m a.s.l.), can be affected by wake effects from the pier deck for onshore east-south-east–south-east wind directions.

Another noteworthy case is associated with the behaviour of the drag coefficient observed at the Video tower for onshore flow between ≈350° and ≈40° (Fig. 6g). Values of C_D ~ 10^{-3} measured by the two upper sonic anemometers (levels 3 and 4) correspond to sea-surface footprints, whereas C_D observed at the two lower levels 1 and 2 are associated with the rough inland footprints. This sharp vertical change in C_D due to the different surface types creates a decoupled boundary-layer system and, in this case, the IBL height is located between the sonic anemometers at levels 2 and 3 (9.4 and 17.9 m above ground level (a.g.l.), respectively, see Table 1). One can assume the remarkable behaviour of C_D at levels 1 and 2 in the sector from ≈350° to ≈40° (Fig. 7d) is due to the influence of the coastal cliff canyon visible at the right-hand side of the Video tower in Fig. 2, which imposes rough boundary-layer characteristics on the flow (Klipp 2007).

The influence of individual obstacles, such as a sharp-edged coastal cliff, is apparent for measurements made within the roughness sublayer at the SDF tower, especially for the sonic anemometer mounted at level 1 (see Figs. 2 and 3d). Turbulent shear flow near the coastal cliff is particularly complex and unsteady. Flow regimes are strongly dependent on the wind direction, and the structure of airflow around a surface obstacle can include a front recirculation zone, flow separation, a corner stream zone, or a wake region (e.g., Coceal and Belcher 2004; Klipp 2007, and references therein). Although this makes interpretation of the turbulent observations at the SDF tower difficult, some universal functions obtained above and within the roughness sublayer are relatively insensitive to local obstructions (see Sect. 4).

The plot of sensible heat flux H_S versus the wind direction (Fig. 6) also shows a strong directional dependence. Positive values of H_S for all four towers are predominantly observed during onshore wind directions, particularly in the sector between 342° and 72° (the prevailing wind sector), which represents unstable or CBL conditions. A negative sensible heat flux $H_S < 0$ associated with the SBL is mainly observed for offshore wind conditions (Fig. 6). These results are generally consistent with the previous observations at Duck, North Carolina reported by Friebel et al. (2009, Fig. 6).

4 Verification and Validation of MOST in the Coastal Zone

The comprehensive CASPER-East dataset enables us to evaluate the classical universal functions of MOST over inhomogeneous surfaces by comparing our data with that collected over flat and homogeneous surfaces during the landmark 1968 Kansas field experiment (e.g., Businger et al. 1971; Dyer 1974; Kaimal and Finnigan 1994).

According to MOST, any properly-scaled statistics of turbulence are universal functions of the Monin-Obukhov stability parameter (4). Specifically, the non-dimensional vertical gradients of mean wind speed U and potential temperature θ can be written as

$$\varphi_m(\zeta) = \left(\frac{\kappa z}{u_*}\right)\frac{dU}{dz} \tag{6a}$$

and

$$\varphi_h(\zeta) = \left(\frac{\kappa z}{\theta_*}\right)\frac{d\theta}{dz} \ , \tag{6b}$$

respectively, where $\theta_* = -\overline{w'\theta'}/u_*$ is the temperature scale. The von Kármán constant κ on the right-hand sides of Eq. 6a, b is conventionally introduced solely as a matter of convenience to ensure $\varphi_m(0) = \varphi_h(0) = 1$ for neutral conditions, $\zeta \equiv 0$. Similarly, the standard deviation of the velocity components σ_α and air temperature σ_θ are scaled as

$$\varphi_\alpha(\zeta) = \frac{\sigma_\alpha}{u_*} \tag{7a}$$

and

$$\varphi_\theta(\zeta) = \frac{\sigma_\theta}{|\theta_*|} \;, \tag{7b}$$

respectively, where α (= u, v, and w) denotes the longitudinal, lateral, and vertical velocity components, respectively. The TKE dissipation rate ε in the MOST framework is expressed as

$$\varphi_\varepsilon(\zeta) = \frac{\kappa z \varepsilon}{u_*^3} \;\;. \tag{8}$$

The exact forms of the universal functions are generally determined using field experiments, although an asymptotic behaviour of these functions under very stable (ζ >> 1) and extremely unstable stratification (free convection, ζ << – 1) conditions can be predicted using self-similarity arguments (e.g., Monin and Yaglom 1971; Stull 1988; Sorbjan 1989; Garratt 1992; Kaimal and Finnigan 1994; Wyngaard 2010). The data presented here were quality controlled prior to evaluating similarity functions (6)–(8) to remove spurious or low-quality records using the same filtering criteria as described in Grachev et al. (2016).

Figure 7 shows the normalized standard deviation of the vertical velocity component $\varphi_w = \sigma_w / u_*$ versus the local Monin-Obukhov stability parameter $\zeta = z/L$, in logarithmic coordinates for turbulent data from the Pier, SDF, SDT and Video towers for all wind directions.

The data were divided into unstable and stable conditions by evaluating the Monin-Obukhov stability parameter at each observational level (local scaling), with the left panels (Fig. 7a, c, e, g) presenting unstable ($\zeta < 0$) conditions and the right panels (Fig. 7b, d, f, h) stable ($\zeta > 0$) conditions. Similar plots of the normalized standard deviation of the longitudinal velocity component $\varphi_u = \sigma_u / u_*$ versus ζ are shown in Fig. 8. According to Figs. 7 and 8, both universal functions $\varphi_w(\zeta)$ and $\varphi_u(\zeta)$ follow MOST predictions (local scaling) with surprisingly small scatter between different towers. Furthermore, the data for different measurement levels at each tower collapse fairly well onto a single universal curve, especially for φ_w (Fig. 7). In particular, as the universal functions $\varphi_w(\zeta)$ and $\varphi_u(\zeta)$ are approximately constant for $\zeta > 0$ according to Figs. 7 and 8, they are consistent with the classical Monin-Obukhov *z*-less scaling (e.g., see Grachev et al. 2013 for discussion). Similar results have also been obtained for the normalized standard deviation of the lateral velocity component $\varphi_v = \sigma_v / u_*$, with $\varphi_v \approx 1.8$ for $|\zeta| \to 0$ (not shown). As expected, the neutral asymptotic limits follow the sequence $\varphi_w(0) < \varphi_v(0) < \varphi_u(0)$, highlighting the anisotropy of the airflow in the near-neutral regime. Our results are consistent with the classical findings of $\varphi_u(0) = 2.39$, $\varphi_v(0) = 1.92$, and $\varphi_w(0) = 1.25$ determined by Panofsky and Dutton (1984) from data collected over flat terrain (over land) for near-neutral stability. Note that the greater scatter of points in Figs. 7c, d and 8c, d for the lower level at the SDF tower results from the proximity of the level-1 sonic anemometer to the coastal terrain and local obstructions (see Figs. 2 and 3d).

The dimensionless standard deviation of the sonic temperature $\varphi_\theta = \sigma_\theta / |\theta_*|$ as a function of ζ for all four towers is plotted in Fig. 9. According to Eq. 7b, φ_θ for near-neutral conditions $|\zeta| \to 0$ is ambiguous (Fig. 9) because the temperature scale θ_* is small and asymptotically tends to zero as ζ approaches zero (e.g., Grachev et al. 2008, their Fig.8). At the same time, σ_θ is small in the near-neutral case but of still a finite value (e.g., Grachev et al. 2003, their Fig. 6b). This behaviour of σ_θ is associated with a thermally-inhomogeneous surface wherein local 'hot' and 'cold' spots on the surface generate small-scale advection, which enhances σ_θ (see discussion in Grachev et al. 2005, p. 221–222; Nadeau et al. 2013, p. 412). While the scatter is larger for the φ_θ case, the data qualitatively follow the MOST canonical curves except for near-neutral and very highly stable cases; that is, φ_θ decreases with decreasing ζ for $\zeta < 0$ and remains approximately constant for $\zeta > 0$. However, our measured φ_θ sit systematically above the curves suggested by Kaimal and Finnigan (1994).

It should be noted that our observations are consistent with previous measurements of the non-dimensional standard deviations over different surface cover types, such as Arctic pack ice with almost unlimited and extremely uniform fetch (e.g., Grachev et al., 2013, 2015), forests (e.g., Rannik 1998; Babić et al. 2016a), rugged mountainous terrain (e.g., Nadeau et al. 2013; Babić et al. 2016b; Grachev et al., 2016; Stiperski and Rotach 2016), and urban areas (e.g., Wood et al. 2010). In other words, it is possible to argue that the above results for different terrain surfaces, including our data, are generally in close qualitative agreement with those reported for flat and homogeneous terrain where MOST applies (at least within the accuracy of the field turbulence data of ≈20–30%).

Figure 10 shows the averaged normalized dissipation rate of TKE φ_ε as defined by Eq. 8, where ε is estimated based on the common method that assumes the existence of an inertial subrange associated with a Richardson-Kolmogorov cascade (see Grachev et al. 2016, Eqs. 5 and 6). Data deviating by more than 20% from the theoretical −5/3 slope in the frequency range 0.49–0.74 Hz, which is located within the inertial subrange, are excluded from the analysis. According to Fig. 10, the scatter among different observation levels for φ_ε is somewhat greater compared with the variables plotted in Figs. 7–9. As mentioned above, data for φ_ε collected at the SDF tower (Fig. 10c, d) show a systematic bias because the sonic anemometers at this tower are located too close to a sand cliff (see Figs. 2 and 3d), and measurements are more affected by coastal terrain.

Previously, we evaluated the similarity of the single-point statistics of turbulence such as the scaled standard deviations and the dissipation rate of TKE, with the normalized standard deviations of the velocity components in the coastal zone agreeing well with the expected MOST predictions (Figs. 7 and 8). Based on the multi-level measurements, we now investigate the relationship between vertical gradients of mean wind speed and potential temperature and turbulent fluxes, which are also known as the flux-profile relationships, and are defined by Eq. 6a, b. All derivatives in (6) are evaluated with a forward finite-difference method in a layer Δz using the sonic anemometers and the slow-response T/RH probes for the wind speed and air temperature, respectively; that is, $dU/dz \approx \Delta U/\Delta z$ and $d\theta/dz \approx \Delta\theta/\Delta z$, respectively. Specifically, the vertical gradients at an intermediate level *n* are based on linear interpolations of the mean wind speed and potential temperature derived from the two adjoining levels *n*–1 and *n*+1; whereas the gradients at the lowermost and uppermost levels are evaluated from the difference at the first two and the last two levels, respectively. Thus, these non-dimensional vertical gradients of mean wind speed and potential temperature are, in fact, bulk variables, as φ_m and φ_h are evaluated in a layer several metres thick. In contrast, the non-dimensional standard deviations and the dissipation rate according to Eqs. 7 and 8, respectively, are local variables because they are measured at a single level.

Figure 11 shows the non-dimensional vertical gradient of mean wind speed φ_m according to Eq. 6a versus $\zeta = z/L$ for the data collected at the Pier, SDF, SDT and Video towers for unstable ($\zeta < 0$) and stable ($\zeta > 0$) conditions and for all wind directions. Similar plots of the non-dimensional vertical gradient of mean potential temperature φ_h according to Eq. 6b versus ζ are shown in Fig. 12. The universal functions φ_m and φ_h are found to vary significantly among different towers and observation levels. The scatter of 30-min values can exceed an order of magnitude, and it appears that the observations in Figs. 11 and 12 do not generally support the classical Businger–Dyer expressions for the non-dimensional profiles of wind speed φ_m and, more egregiously, the air temperature φ_h. Other studies have also shown flux-variance similarity to be more successful than flux-gradient similarity. For example, Rannik (1998) reached this conclusion with eddy-covariance data collected over a pine forest and Nadeau et al. (2013) over a steep Alpine slope.

Note that some of the plots, e.g., φ_m versus ζ (Fig. 11), are affected by self-correlation because the same variables (primarily the friction velocity u_*) appear in both the definitions of the universal functions and the dependent variable ζ on which a functional relationship is sought, resulting, for example, in a weak trend of the data in Figs. 7 and 8 for $\zeta > 0$ (cf. Grachev et al. 2013, Fig. 15; Grachev et al. 2016, Fig. 10). However, the self-correlation can be overcome, for example, by plotting a universal function or stability parameter in a "hybrid" representation without u_* (see Grachev et al. 2013, Fig. 16; Grachev et al. 2015, p. 1854; Babić et al. 2016a, Fig. 14; Stiperski and Rotach 2016, p. 116 for discussion), which is based on the idea that a combination of any Monin-Obukhov universal functions is itself a universal function. For example, the terms $\varphi_m\varphi_w^{-1}$, $\varphi_\varepsilon\varphi_w^{-3}$, $\varphi_w\varphi_u^{-1}$ among others plotted versus ζ by definition are not affected by the self-correlation because the "new" universal function shares no variables with ζ (except a measurement height z in some cases). To test the sensitivity of our results to self-correlation, Fig. 13 shows plots as presented in Fig. 11, but for the universal function $\varphi_m \varphi_w^{-1} = \left(\frac{\kappa z}{\sigma_w} \right) \frac{dU}{dz}$ (formally u_* in Eq. 6a is replaced by σ_w) which do not contain flaws associated with self-correlation as found in Fig. 11. According to Fig. 13, the scatter of the data around the empirical Kansas-type expressions reported by Kaimal and Finnigan (1994) does not change substantially, so that the self-correlation likely would not affect our overall results.

Although the scatter plots of universal functions presented in Figs. 7–13 are useful tools to depict individual data points, overall trends, as well as the typical degree of scatter, additional detailed information is obtained from bin-averaged data. Figures 14 and 15 show the bin-averaged dependencies of the non-dimensional functions φ_w, φ_ε, φ_m, and φ_h observed at different levels versus $\zeta = z / L$ for the data collected over water at the Pier tower and over land at the Video tower, respectively, for both unstable ($\zeta < 0$) and stable ($\zeta > 0$) conditions and, separately, for onshore and offshore flow (see Sect. 3.2 for the definition of the onshore/offshore wind directions). Note that the universal functions in Figs. 14 and 15 are represented in logarithmic-linear coordinates (cf. plots of these functions in Figs. 7–12).

According to Fig. 14a and b, the bin-averaged data for φ_w observed at different levels during onshore flow (colour solid lines) collapse fairly well onto a single universal curve, implying the dimensionless vertical velocity variance to be a universal function of ζ. Therefore, one may assume φ_w closely follows the canonical Monin-Obukhov predictions, which are generally valid for flat and homogeneous terrain, although CASPER-East data for φ_w underestimates the empirical Kansas-type expressions reported by Kaimal and Finnigan (1994, Eq. 1.33) for unstable conditions in the range $-1 < \zeta < -0.01$ (Fig. 14a). However, our observations of φ_w better support the Kansas-type relationship for stable conditions (Fig. 14b), which is possibly due to the fact that stable stratification inhibits vertical motion, and the turbulence no longer communicates effectively with the surface (the *z*-less concept; see Grachev et al. 2013 for discussion). The bin-averaged values of φ_w for offshore flow (colour dashed lines) show larger scatter among different observation levels, and generally exceed the values of φ_w observed for onshore flow (Fig. 14a, b).

The bin-averaged curves for the normalized dissipation rate of TKE φ_ε (Fig. 14c, d) behave very similarly to φ_w (Fig. 14a, b) as evident in the good collapse of the coloured solid lines in Fig. 14c, d onto a single universal curve, but the Kansas-type expressions reported by Kaimal and Finnigan (1994, Eq. 1.35) overpredict the bin-averaged data for φ_ε in the range $-1 < \zeta < -0.01$. One may accordingly argue that φ_ε generally follows MOST scaling, but with a larger scatter of the individual 30-min-averaged data points than φ_w (cf. Figs. 7 and 10). Note that data for φ_w and φ_ε collected at level 1 (Fig. 14) may in certain situations be affected by the pier deck and other structures located on the pier (see Figs. 1 and 3a), especially for offshore flow. Some data under very stable conditions (Fig. 14b, d) are beyond the limits of the applicability for similarity theory in stable conditions (e.g., Grachev et al. 2013; Babić et al. 2016a), and such data may also be biased by the inclusion of non-turbulent motions.

The above results for φ_w and φ_ε at the Pier tower are also valid for the universal functions observed over land at the Video tower for levels 3 and 4 in the case of onshore flow (Fig. 15), because the two upper sonic anemometers (levels 3 and 4) correspond to sea-surface footprints, whereas φ_w and φ_ε observed at the two lower levels 1 and 2 are associated with the rough inland footprints (see discussion in Sect. 3.2).

Figures 14e–h and 15e–h show bin-averaged flux-profile relationships versus $\zeta = z/L$ for the Pier and Video towers, respectively. In contrast to the φ_w and φ_ε functions (Figs. 14a–d and 15a–d), our observations in the coastal zone show poor correspondence to either the classical Monin-Obukhov predictions or Businger–Dyer expressions (black dashed lines in Figs. 14e–h and 15e–h) for the non-dimensional profiles of mean wind speed φ_m and mean temperature φ_h. First, the bin-averaged values of φ_m and φ_h measured at different levels (coloured solid and dashed lines in Figs. 14e–h and 15e–h) do not collapse onto a single curve, even for onshore flow at the Pier tower (Figs. 14e–h). Second, there are negative values of φ_m and φ_h due to negative wind-speed and temperature gradients, implying that the vertical components of the turbulent fluxes are counter to the mean gradients, which is incompatible with the requirement of MOST of positive turbulent viscosity $k_m = -\frac{\overline{u'w'}}{dU/dz}$ and thermal diffusivity $k_h = -\frac{\overline{w'\theta'}}{d\theta/dz}$. Overall, the dependence of φ_m and φ_h on $\zeta = z/L$ appears weak, if not non-existent. We note, however, that their qualitative behaviour versus ζ is better for φ_m than for φ_h, as the bin-averaged data for different measurement levels at each tower for φ_m collapse better onto a single curve.

It is possible that different the behaviour of various universal functions are associated with a combination of local and non-local turbulent transport in the ABL. Estimates of the non-dimensional standard deviations (7) and the dissipation rate (8) are based on a single level of turbulence measurements, and depend heavily on small-scale turbulent mixing (high-frequency turbulent motions). At these scales, the small eddies adapt quickly to changes in the large-scale conditions (e.g., variations in the coastal terrain), and thereby maintain a dynamic equilibrium with the specific TKE and the dissipation rate imposed by the large eddies. Because MOST is a generalization of mixing-length theory for small-scale turbulence in non-neutral conditions, it is reasonable to expect that the scaled standard deviations (7) and the dissipation rate (8) generally obey MOST, even in inhomogeneous regions such as coastal zones. At the same time, estimates of the vertical gradients of mean wind speed and potential temperature in φ_m and φ_h (see Eq. 6) are based on measurements in a layer Δz several metres thick as mentioned earlier, since the derivatives in (6) are bulk variables. The bulk vertical mean gradients are controlled by both small-scale eddy diffusion and large-scale motions driven by pressure gradients, uneven surface heating, etc, besides large-scale eddies may also be constrained by the IBL height and the coastal terrain geometry. These larger-size eddies can transport momentum and heat throughout the entire depth of the ABL (nonlocal mixing) and, under such conditions, vertical fluxes can be counter to local gradients. It is thus evident that non-local transport in the ABL is overlooked by traditional MOST.

In a similarity-theory framework, the above statement can be formulated as a generalized approach, with classical MOST as a special case (e.g., Johansson et al. 2001; Wilson 2008). A more general formulation of similarity theory ('extended MOST') includes additional influences on the flux-gradient relationships (or flux-variance, etc.) to the parameters considered in traditional MOST; for example, the Coriolis parameter, boundary-layer depth, upwind fetch, aerodynamic and scalar roughness lengths, molecular viscosity, and thermal conductivity. According to Buckingham's Pi theorem, such extra parameters lead to more independent dimensionless π groups (see Grachev et al. 2015 for discussion)

$$\pi = f\left(\pi_1, \pi_2, \pi_3, ...\right), \qquad (9)$$

where the first π group in (9) is based on the MOST governing parameters and z leads to $\pi_1 = z/L$, which is defined as the ratio of the measurement height z to the Obukhov length scale L (see Eq. 4). The other dimensionless groups contain the ABL (or IBL) depth h and fetch x (upwind distance), giving $\pi_2 = h/L$ and $\pi_3 = xg/U^2$, respectively. One may suggest that in the case of $\pi = \varphi_w$, the normalized standard deviation of the vertical velocity component $\varphi_w = \sigma_w / u_*$ is insensitive to the dimensionless parameters π_2, π_3, etc. In this case, Eq. (9) reduces to $\varphi_w = f(\pi_1)$, implying $\varphi_w = \sigma_w / u_*$ is consistent with classical MOST predictions. At the same time, the π_2 and π_3 groups, supposedly, cannot be neglected for $\pi = \varphi_m$ and $\pi = \varphi_h$ in the coastal zone (cf. Johansson et al. 2001), leading to a poor correspondence with MOST for the flux-profile relationships.

A similar situation has already been described in the literature for the dimensionless standard deviations φ_u, φ_v, and φ_w, which behave differently in the CBL (e.g., Panofsky et al. 1977; Sorbjan 1989; Johansson et al. 2001; Wilson 2008; Nadeau et al. 2013; Babić et al. 2016b). According to Panofsky et al. (1977), the normalized standard deviations of the horizontal velocity components φ_u and φ_v in the surface layer under convective conditions are influenced by boundary-layer scale eddies and, therefore, both should be a function of $\pi_2 = h/L$, where *h* is the height of the lowest inversion. At the same time, Panofsky et al. (1977) found that φ_w obtained from the same experiments scales with $\pi_1 = z/L$ in good agreement with MOST.

5 Summary and Discussion

We analyzed data of small-scale atmospheric turbulence collected at the U.S. Army Corps of Engineers FRF during the CASPER-East Program from 8 October through 9 November 2015. This site is located on the Outer Banks between the Atlantic Ocean and the Currituck Sound near the town of Duck, North Carolina. Turbulence and mean meteorological data were collected at multiple (from two to four) levels on four towers (Fig. 1), with three towers, namely the "Video" (or "Tall"), "Sand Dune Top" (SDT), and "Sand Dune Foot" (SDF) towers, deployed on land at progressive distances from the shoreline (Figs. 1, 2, 3b, c and d). A fourth tower, called the "Pier tower", was located at the end of the 560-m-long FRF pier (Figs. 1 and 3a). The CASPER-East measurements facilitate a detailed analysis of the temporal and spatial structure of the ABL in the FRF coastal zone, and provide insights into the nature of the air–sea/land coupling. In particular, the observations enable comparison of the turbulent fluxes and other turbulence statistics, as well as different scaling laws for turbulent mixing over a variety of footprints, including a relatively smooth sea surface and aerodynamically-rough dry inland areas.

We first analyze the time series of 30-min-averaged turbulent fluxes and basic meteorological variables. According to the results shown in Fig. 4, the occurrence of a sea–land breeze system in the FRF coastal area during the field campaign was observed with wind speeds less than 4–5 ms^{-1}. Both stable ($\zeta > 0$) and unstable ($\zeta < 0$) stratification was observed over the water (Fig. 5g) and land (Fig. 5h). Although the time series of various turbulent fluxes are very similar for sea and land footprints, there are noticeable differences associated with the different aerodynamic and thermal properties of the underlying surfaces. For example, we find that the friction velocity observed at the Pier tower is generally less than at the Video tower, because the ocean has a relatively smooth surface (Fig. 5a and b). In addition, the 30-min-averaged drag coefficient over land-footprint areas can be an order of magnitude larger than over the sea surface due to the change in aerodynamic properties of the surface (see Fig. 6). Another marked difference is a well-pronounced diurnal cycle in sensible heat observed at the Video tower (Fig. 5d) due to a different heat capacity between the water and land. Generally, the drag coefficient and diurnal variation of sensible heat flux can be considered as indicators for different types of surface footprints.

For onshore flow, the IBL in the coastal zone can be stable or (more usually) unstable (Fig. 6), and vary dramatically at the coastal land-surface discontinuity. Measurements from the Video tower for onshore flow in the sector from ≈350° to ≈40° show an IBL height located between the sonic anemometers at levels 2 and 3 (between 9.4 and 17.9 m a.g.l.), because the values of $C_D \sim 10^{-3}$ measured by the two upper sonic anemometers (levels 3 and 4) correspond to sea-surface footprints, whereas C_D observed at the two lower levels 1 and 2 is associated with the rough, inland footprints (Fig. 6g). Conversely, for offshore flow of generally warm air over a cooler sea surface, a stable IBL develops over the ocean surface downstream from the shore (Fig. 6).

We focused primarily on the applicability of MOST in the coastal zone, with non-dimensional terms according to MOST calculated from 30-min-averaged data and plotted versus $\zeta = z/L$ for both unstable and stable conditions (Figs. 7–12). We then analyzed the dependence of bin-averaged data scaled according to MOST versus ζ for measurements over water and land for both onshore and offshore flow (Figs. 14 and 15). Scatter plots of the individual 30-min-averaged values of the scaled universal functions presented in Figs. 7–10 demonstrate that the non-dimensional standard deviations (7) and the dissipation rate (8) generally obey MOST quite well for all locations (maybe with the exception of the SDF tower due to local interferences), stability conditions, and wind direction. However, the data scatter for φ_ε (Fig. 10) is somewhat greater compared with that for the normalized standard deviations (Figs. 7–9). The deviation of φ_θ values from the MOST canonical curves in near-neutral conditions (Fig. 9) is likely associated with an inhomogeneous surface temperature (see the discussion in Sect. 4). Note also that, statistically, the dependence on ζ is better for φ_w (Fig. 7) than for φ_u (Fig. 8). A more thorough analysis of the bin-averaged data plotted in logarithmic-linear coordinates shows that φ_w calculated from the Pier tower data (Fig. 14a, b) collapses better onto a single universal curve for onshore than for offshore flow. The bin-averaged data also show that the Kansas-type expressions reported by Kaimal and Finnigan (1994, Eqs. 1.33 and 1.35) overpredict the bin-averaged observations of both φ_w and φ_ε in the range $-1 < \zeta < -0.01$ (Figs. 14a, c and 15a, c).

In contrast to the single-point statistics of turbulence, such as the scaled standard deviations and the dissipation rate (Figs. 14a–d and 15 a–d), our observations for the non-dimensional gradients of wind speed φ_m and temperature φ_h in the coastal zone (Figs. 13, 14, 14e–h, and 15e–h), show poor correspondence to both the classical Monin-Obukhov predictions and Businger–Dyer expressions (Kaimal and Finnigan 1994, Eqs. 1.31 and 1.31). According to Figs. 11 and 12, the individual 30-min-averaged values of φ_m and φ_h are found to vary significantly among different towers and observation levels, and the scatter of measurements can exceed one order of magnitude. Overall, the statistical dependence of φ_m and φ_h on ζ appears weak, if not non-existent. One may assume that these results (especially for onshore flow) should be generally applicable for other similar sites located within a coastal zone.

We argue that such dissimilar behaviour of different universal functions may be associated with a combination of local and non-local turbulent mixing in the ABL. The scaled standard deviations (7) and the dissipation rate (8), which generally obey MOST, are based on single-level turbulence measurements, and are mostly associated with those high-frequency turbulent motions (small-scale eddies) that are somewhat uncorrelated with larger-scale motions. This small-scale turbulence depends heavily on the local properties of the airflow, such as local (small-scale) gradients/fluxes and stratification, with less dependence on larger-scale forcing. In contrast, the flux-profile relationships (6), where the vertical gradients of the mean wind speed and potential temperature are based on coarse-resolution measurements in a layer of several metres thickness ("bulk gradients"), are controlled by both small-scale eddies, as well as mesoscale circulation in the ABL. Thus, the classical relationships (6) are inappropriate for describing the non-dimensional gradients of wind speed and temperature in a coastal zone because non-local transport is not considered by traditional MOST. While the use of highly-resolved dU/dz and $d\theta/dz$ in (6) may lead to an improved correspondence of φ_m and φ_h with canonical MOST functions, further investigations are needed to verify this hypothesis.

Acknowledgements The CASPER Program was funded by the Office of Naval Research (ONR) under its Multidisciplinary University Research Initiative (MURI) program, grant N0001416WX00469 to NPS and grant N00014-17-1-3195 to University of Notre Dame, with program managers Dr. Daniel Eleuterio and Dr. Steve Russell. We thank all the researchers who organized, deployed, operated, and maintained the instruments that have provided the in situ measurements during the CASPER-East field campaign. Their efforts are greatly appreciated.

References

Alappattu DP, Wang Q, Yamaguchi R, Lind RJ, Reynolds M, Christman AJ (2017) Warm layer and cool skin corrections for bulk water temperature measurements for air-sea interaction studies. J Geophys Res Oceans 122(C8):6470-6481 DOI: 10.1002/2017JC012688

Andreas EL (2002) Parameterizing scalar transfer over snow and ice: A review. J Hydrometeorol 3(4): 417–432

Atkinson BW, Zhu M (2005) Radar-duct and boundary-layer characteristics over the area of The Gulf. Q J R Meteorol Soc 131(609A):1923–1953 DOI: 10.1256/qj.04.113

Babić K, Rotach MW, Klaić ZB (2016a) Evaluation of local similarity theory in the wintertime nocturnal boundary layer over heterogeneous surface. Agric Forest Meteorol 228–229:164–179 DOI: 10.1016/j.agrformet.2016.07.002

Babić N, Večenaj Ž, De Wekker SFJ (2016b) Flux-variance similarity in complex terrain and its sensitivity to different methods of treating non-stationarity. Boundary-Layer Meteorol 159(1):123–145 DOI: 10.1007/s10546-015-0110-0

Brooks IM (2001) Air-sea interaction and spatial variability of the surface evaporation duct in a coastal environment. Geophys Res Lett 28(10):2009–2012 DOI: 10.1029/2000GL012751

Brooks IM, Goroch AK, Rogers DP (1999) Observations of strong surface radar ducts over the Persian Gulf. J Appl Meteorol 38(9):1293–1310

Burba G (2013) Eddy covariance method for scientific, industrial, agricultural and regulatory applications: A field book on measuring ecosystem gas exchange and areal emission rates. LI-COR Biosciences, Lincoln, USA, 331 pp. ISBN: 978-0-61576827-4

Businger JA, Wyngaard JC, Izumi Y, Bradley EF (1971) Flux-profile relationships in the atmospheric surface layer. J Atmos Sci 28:181–189

Coceal O, Belcher SE (2004) A canopy model of mean winds through urban areas. Q J R Meteorol Soc 130(599):1349–1372. DOI: 10.1256/qj.03.40

Dolan R, Lins HF (1986) The Outer Banks of North Carolina: U.S. Geological Survey Professional Paper 1177-B, 49 pp. DOI: 10.3133/pp1827 (available at: https://pubs.usgs.gov/pp/1177b/report.pdf)

Dolan R, Lins HF, Smith JJ (2016) The Outer Banks of North Carolina: U.S. Geological Survey Professional Paper 1827, 153 pp. DOI: 10.3133/pp1827 (available at: https://pubs.er.usgs.gov/publication/pp1827)

Dyer AJ (1974) A review of flux-profile relationships. Boundary-Layer Meteorol 7:363–372

Fairall CW, Bradley EF, Hare JE, Grachev AA, Edson JB (2003) Bulk parameterization of air-sea fluxes: updates and verification for the COARE algorithm. J Climate 16(4):571–591

Fairall CW, Bariteau L, Grachev AA, Hill RJ, Wolfe DE, Brewer WA, Tucker SC, Hare JE, Angevine WM (2006) Turbulent bulk transfer coefficients and ozone deposition velocity in the International Consortium for Atmospheric Research into Transport and Transformation. J Geophys Res 111(D23):D23S20. DOI: 10.1029/2006JD007597

Friebel HC, Hanson JL, Benilov AY, Resio DT (2009) Long-term drag coefficient measurements in the coastal zone. 11th International Workshop on Hindcasting and Forecasting and 2nd Coastal Hazard Symposium. Halifax, NS, Canada October 18-23, 2009, JCOMM Technical Report 52, WMO/TD-No. 1533, IOC Workshop Report 232 (available at: http://www.waveworkshop.org/11thWaves/Papers/FriebelEtAl_Halifax_1Oct09.pdf)

Garratt JR (1987) The stably stratified internal boundary-layer for steady and diurnally varying offshore flow. Boundary-Layer Meteorol 38(4):369–394. DOI: 10.1007/BF00120853

Garratt JR (1990) The internal boundary-layer – A review. Boundary-Layer Meteorol 50(1):171–203. DOI: 10.1007/BF00120524

Garratt JR (1992) The Atmospheric Boundary Layer. Cambridge University Press, UK 316 pp

Garratt JR, Ryan BF (1989) The structure of the stably stratified internal boundary-layer in offshore flow over the sea. Boundary-Layer Meteorol 47(1):17–40. DOI: 10.1007/BF00122320

Geernaert GL (1988) Drag coefficient modelling for the near-coastal zone. Dyn Atmos Oceans 11(3-4):307–322. DOI: 10.1016/0377-0265(88)90004-8

Geernaert GL (2002) On extending the flux-profile similarity theory to include quasi-homogeneous conditions in the marine atmospheric surface layer. Boundary-Layer Meteorol 105(3):433–450. DOI: 10.1023/A:1020307703242

Geernaert GL (2007) On the evaporation duct for inhomogeneous conditions in coastal regions. J Appl Meteorol Climatol 46(4):538–543 DOI: 10.1175/JAM2481.1

Geernaert GL (2010) Normalizing air-sea flux coefficients for horizontal homogeneity, stationarity, and neutral stratification. J Phys Oceanogr 40(9):2148–2158 DOI: 10.1175/2010JPO4407.1

Glazunov A, Rannik Ü, Stepanenko V, Lykosov V, Auvinen M, Vesala T, Mammarella I (2016) Large-eddy simulation and stochastic modeling of Lagrangian particles for footprint determination in the stable boundary layer. Geosci Model Dev 9:2925-2949 DOI: 10.5194/gmd-9-2925-2016.

Grachev AA, Fairall CW, Larsen SE (1998) On the determination of the neutral drag coefficient in the convective boundary layer. Boundary-Layer Meteorol 86(2):257–278 DOI: 10.1023/A:1000617300732

Grachev AA, Fairall CW, Persson POG, Andreas EL, Guest PS, Jordan RE (2003) Turbulence decay in the stable arctic boundary layer. American Meteorological Society, Seventh Conference on Polar Meteorology and Oceanography and Joint Symposium on High-Latitude Climate Variations. 12–16 May 2003, Hyannis MA, Paper 3.12 (http://ams.confex.com/ams/7POLAR/techprogram/paper_61456.htm)

Grachev AA, Fairall CW, Persson POG, Andreas EL, Guest PS (2005) Stable boundary-layer scaling regimes: The SHEBA data. Boundary-Layer Meteorol 116(2):201–235 DOI: 10.1007/s10546-004-2729-0

Grachev AA, Andreas EL, Fairall CW, Guest PS, Persson POG (2008) Turbulent measurements in the stable atmospheric boundary layer during SHEBA: Ten years after. Acta Geophys 56(1):142–166. DOI: 10.2478/s11600-007-0048-9

Grachev AA, Bariteau L, Fairall CW, Hare JE, Helmig D, Hueber J, Lang EK (2011) Turbulent fluxes and transfer of trace gases from ship-based measurements during TexAQS 2006. J Geophys Res 116(D13):D13110 DOI: 10.1029/2010JD015502

Grachev AA, Andreas EL, Fairall CW, Guest PS, Persson POG (2013) The critical Richardson number and limits of applicability of local similarity theory in the stable boundary layer. Boundary-Layer Meteorol 147(1):51–82. DOI: 10.1007/s10546-012-9771-0

Grachev AA, Andreas EL, Fairall CW, Guest PS, Persson POG (2015) Similarity theory based on the Dougherty-Ozmidov length scale. Q J R Meteorol Soc 141(690A):1845–1856 DOI: 10.1002/qj.2488

Grachev AA, Leo LS, Di Sabatino S, Fernando HJS, Pardyjak ER, Fairall CW (2016) Structure of turbulence in katabatic flows below and above the wind-speed maximum. Boundary-Layer Meteorol 159(3):469–494 DOI: 10.1007/s10546-015-0034-8

Högström U (1988) Non-dimensional wind and temperature profiles in the atmospheric surface layer: A re-evaluation. Boundary-Layer Meteorol 42(1): 55–78 DOI: 10.1007/BF00119875

Horst TW, Weil JC (1992) Footprint estimation for scalar flux measurements in the atmospheric surface layer. Boundary-Layer Meteorol 59(3): 279–296. DOI: 10.1007/BF00119817

Horst TW, Weil JC (1994) How far is far enough?: The fetch requirements for micrometeorological measurement of surface fluxes. J Atmos Ocean Tech 11(4):1018–1025

Johansson C, Smedman A-S, Högström U, Brasseur JG, Khanna S (2001) Critical test of the validity of Monin–Obukhov similarity during convective conditions. J Atmos Sci 58(12):1549–1566

Kaimal JC, Finnigan JJ (1994) Atmospheric boundary layer flows: Their structure and measurements. Oxford University Press, New York and Oxford, 289 pp

Katsaros KB, Smith SD, Oost WA (1987) HEXOS – Humidity Exchange over the Sea, a program for research on water-vapor and droplet fluxes from sea to air at moderate to high wind speeds. Bull Amer Meteorol Soc 68(5):466–476

Klaassen W, Sogachev A (2006) Flux footprint simulation downwind of a forest edge. Boundary-Layer Meteorol 121(3):459–473 DOI: 10.1007/s10546-006-9078-0

Kljun N, Calanca P, Rotach MW, Schmid HP (2004) A simple parameterisation for flux footprint predictions. Boundary-Layer Meteorol 112(3):503–523 DOI: 10.1023/B:BOUN.0000030653.71031.96

Kljun N, Calanca P, Rotach MW, Schmid HP (2015) A simple two-dimensional parameterisation for flux footprint prediction (FFP). Geosci Model Dev 8:3695–3713 DOI: 10.5194/gmd-8-3695-2015

Klipp C (2007) Wind direction dependence of atmospheric boundary layer turbulence parameters in the urban roughness sublayer. J Appl Meteorol Climatol 46(12):2086–2097 DOI: 10.1175/2006JAMC1298.1

Kormann R, Meixner FX (2001) An analytical footprint model for non-neutral stratification. Boundary-Layer Meteorol 99(2):207–224 DOI: 10.1023/A:1018991015119

Leclerc MY, Foken T (2014) Footprints in Micrometeorology and Ecology. Springer-Verlag Berlin Heidelberg, 239 pp DOI: 10.1007/978-3-642-54545-0

Mahrt L (1996) The bulk aerodynamic formulation over heterogeneous surfaces. Boundary-Layer Meteorol 78(1-2):87–119 DOI: 10.1007/BF00122488

Mahrt L, Vickers D, Howell J, Højstrup J, Wilczak JM, Edson J, Hare J (1996) Sea surface drag coefficients in the Risø Air Sea Experiment. J Geophys Res 101(C6):14,327–14,335 DOI: 10.1029/96JC00748

Mahrt L, Vickers D, Edson J, Sun J, Højstrup J, Hare J, Wilczak JM (1998) Heat flux in the coastal zone. Boundary-Layer Meteorol 86(3):421–446 DOI: 10.1023/A:1000784219817

Mahrt L (1999) The Coastal Zone. In Air-sea exchange: Physics, chemistry and dynamics (Ed. G.L. Geernaert), Kluwer Academic Publishers, Dordrecht, pp. 247–268

Mahrt L, Vickers D, Edson J, Wilczak JM, Hare J, Højstrup J (2001a) Vertical structure of turbulence in offshore flow during RASEX. Boundary-Layer Meteorol 100(1):47–61 DOI: 10.1023/A:1018982828967

Mahrt L, Vickers D, Sun J, Crawford TL, Crescenti G, Frederickson P (2001b) Surface stress in offshore flow and quasi-frictional decoupling. J Geophys Res 106(D18): 20,629–20,639 DOI: 10.1029/2000JD000159

Mahrt L, Andreas EL, Edson JB, Vickers D, Sun J, Patton EG (2016) Coastal zone surface stress with stable stratification. J Phys Oceanogr 46(1):95–105 DOI: 10.1175/JPO-D-15-0116.1

Monin AS, Obukhov AM (1954) Basic laws of turbulent mixing in the surface layer of the atmosphere. Trudy Geofiz Inst Acad Nauk SSSR. 24(151):163–187

Monin AS, Yaglom AM (1971) Statistical fluid mechanics: Mechanics of turbulence, Vol. 1, MIT Press, Cambridge, Mass. 769 pp

Nadeau DF, Pardyjak ER, Higgins CW, Parlange MB (2013) Similarity scaling over a steep alpine slope. Boundary-Layer Meteorol 147(3):401–419 DOI: 10.1007/s10546-012-9787-5

Obukhov AM (1946) Turbulence in an atmosphere with a non-uniform temperature. Trudy Inst Teoret Geofiz Akad. Nauk SSSR 1:95–115 (translation in: Boundary-Layer Meteorol, 1971, 2:7–29)

Panofsky HA, Dutton JA (1984) Atmospheric turbulence: models and methods for engineering applications. Wiley, New York, 389 pp

Panofsky HA, Tennekes H, Lenschow DH, Wyngaard JC (1977) The characteristics of turbulent velocity components in the surface layer under convective conditions. Boundary-Layer Meteorol 11(3):355–361 DOI: 10.1007/BF02186086

Rannik Ü (1998) On the surface layer similarity at a complex forest site. J Geophys Res 103(D8):8685–8697 DOI: 10.1029/98JD00086

Smedman A-S, Bergström H, Högström U (1995) Spectra, variances and length scales in a marine stable boundary layer dominated by a low level jet. Boundary-Layer Meteorol 76(3):211–232 DOI: 10.1007/BF00709352

Smedman A-S, Bergström H, Grisogono B (1997a) Evolution of stable internal boundary layers over a cold sea. J Geophys Res 102(C1):1091–1099 DOI: 10.1029/96JC02782

Smedman A-S, Högström U, Bergström H (1997b) The turbulence regime of a very stable marine airflow with quasi-frictional decoupling. J Geophys Res 102(C9):21,049–21,059 DOI: 10.1029/97JC01070

Smith SD, Anderson RJ, Oost WA, Kraan C, Maat N, DeCosmo J, Katsaros K, Davidson KL, Bumke K, Hasse L, Chadwick HM (1992) Sea surface wind stress and drag coefficients: The HEXOS results. Boundary-Layer Meteorol 60(1-2):109–142. DOI: 10.1007/BF00122064

Sorbjan Z (1989) Structure of the atmospheric boundary layer. Prentice-Hall, Englewood Cliffs, NJ, 317 pp

Stiperski I, Rotach MW (2016) On the measurement of turbulence over complex mountainous terrain. Boundary-Layer Meteorol 159(1):97–121 DOI: 10.1007/s10546-015-0103-z

Stull RB (1988) An introduction to boundary-layer meteorology. Kluwer Academic Publishers, Boston, Mass., 666 pp

Sun J, Vandemark D, Mahrt L, Vickers D, Crawford T, Vogel C (2001) Momentum transfer over the coastal zone. J Geophys Res 106(D12):12,437–12,448 DOI: 10.1029/2000JD900696.

Vickers D, Mahrt L (1997) Fetch limited drag coefficients. Boundary-Layer Meteorol 85(1):53–79 DOI: 10.1023/A:1000472623187

Vickers D, Mahrt L (1999) Observations of non-dimensional wind shear in the coastal zone. Q J R Meteorol Soc 125(559A):2685–2702 DOI: 10.1002/qj.49712555917

Vickers D, Mahrt L (2010) Sea-surface roughness lengths in the midlatitude coastal zone. Q J R Meteorol Soc. 136(649B):1089–1093 DOI: 10.1002/qj.617

Vickers D, Mahrt L, Sun J, Crawford T (2001) Structure of offshore flow. Mon Weather Rev 129(5):1251–1258

Wang Q, Alappattu DP, Billingsley S, Blomquist B, Burkholder RJ, Christman AJ, Creegan ED, de Paolo T, Eleuterio DP, Fernando HJS, Franklin KB, Grachev AA, Haack T, Hanley TR, Hocut CM, Holt TR, Horgan K, Jonsson HH, Hale RA, Kalogiros JA, Khelif D, Leo LS, Lind RJ, Lozovatsky I, Panella-Morato J, Mukherjee S, Nuss WA, Pozderac J, Rogers LT, Savelyev I, Savige DK, Shearman RK, Shen L, Terrill E, Ulate AM, Wang Q, Wendt RT, Wiss R, Woods RK, Xu L, Yamaguchi RT, Yardim C (2017) CASPER: Coupled Air-Sea Processes and Electromagnetic (EM) Wave ducting Research. Bull Am Meteorol Soc (accepted).

Wilson JD (2008) Monin-Obukhov functions for standard deviations of velocity. Boundary-Layer Meteorol 129(3):353–369. DOI: 10.1007/s10546-008-9319-5

Wilson JD (2015) Computing the flux footprint. Boundary-Layer Meteorol 156(1):1–14 DOI: 10.1007/s10546-015-0017-9

Wood CR, Lacser A, Barlow JF, Padhra A, Belcher SE, Nemitz E, Helfter C, Famulari D, Grimmond CSB (2010) Turbulent flow at 190 m height above London during 2006–2008: A climatology and the applicability of similarity theory. Boundary-Layer Meteorol 137(1): 77–96 DOI: 10.1007/s10546-010-9516-x

Wyngaard JC (2010) Turbulence in the atmosphere. Cambridge University Press, New York, 393 pp

Table 1. Instrumentation of the four FRF flux towers

Parameter	Instrument	Measurement heights
Pier Tower		
Velocity and sonic temperature	R.M. Young (Model 81000) sonic anemometer	9.9, 13.2, and 17.9 m a.s.l. (Levels 1 to 3) [*]
Air temperature and relative humidity (T/RH)	Campbell Scientific T/RH probe (Model HC2S3)	9.8, 13.1, and 17.9 m a.s.l. (Levels 1 to 3)
Water vapour and carbon dioxide	Open path infrared gas analyzer (Model LI-7500A), LI-COR Inc.	9.9 m a.s.l.
Video (Tall) Tower		
Velocity and sonic temperature	R.M. Young (Model 81000) sonic anemometer	5.1, 9.4, 17.9, and 26.5 m a.g.l. (Levels 1 to 4)
Air temperature and relative humidity (T/RH)	Campbell Scientific T/RH probe (Model HC2S3)	4.7, 8.9, 17.5, and 26 m a.g.l. (Levels 1 to 4)
Sand Dune Top (SDT) Tower		
Velocity and sonic temperature	R.M. Young (Model 81000) sonic anemometer	2.0, 4.7, 6.2 m a.g.l. (Levels 1 to 3)
Air temperature and relative humidity (T/RH)	Campbell Scientific T/RH probe (Model HC2S3)	1.9 and 6.0 m a.g.l.
Water vapour and carbon dioxide	Open path infrared gas analyzer (Model LI-7500A), LI-COR Inc.	2.0 m a.g.l.
Sand Dune Foot (SDF) Tower		
Velocity and sonic temperature	R.M. Young (Model 81000) sonic anemometer	2.0 and 5.9 m a.g.l.
Air temperature and relative humidity (T/RH)	Campbell Scientific T/RH probe (Model HC2S3)	1.9 and 6.1 m a.g.l.

[*] An additional sonic anemometer was installed at the Pier tower on 30 October at a measurement height of 7.47 m a.s.l. ("Level 0").

Fig 1 Aerial view of the U.S. Army Corps of Engineers Field Research Facility (FRF) showing the 560-m long pier together with the positions of the four towers (shown as stars) as part of the coastal-zone experimental set-up during the CASPER-East field campaign. The facility is located on the Outer Banks near the town of Duck, North Carolina and stretches from the Atlantic Ocean in the east (lower-left portion of the picture) to the Currituck Sound west of the facility (upper right). Photo credit: FRF.

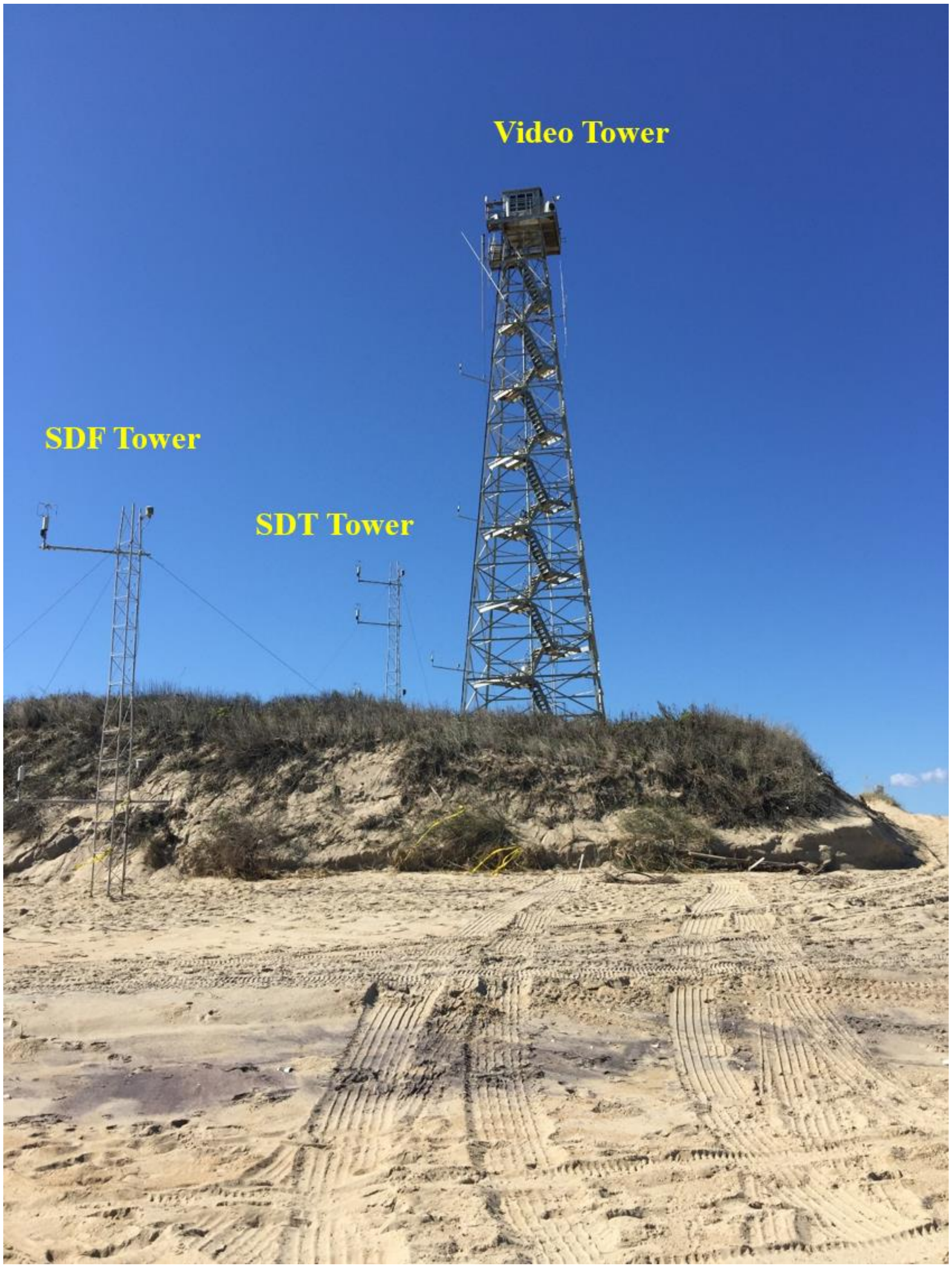

Fig 2 View from the Atlantic Ocean of the three instrumented shore towers, named (from left to right) the Sand Dune Foot (SDF), Sand Dune Top (SDT), and Video towers. Photo credit: Andrey Grachev.

Fig. 3 View of the (*a*) Pier, (*b*) Video, (*c*) SDT, and (*d*) SDF towers and instruments during the CASPER-East campaign. Photo credit: Andrey Grachev.

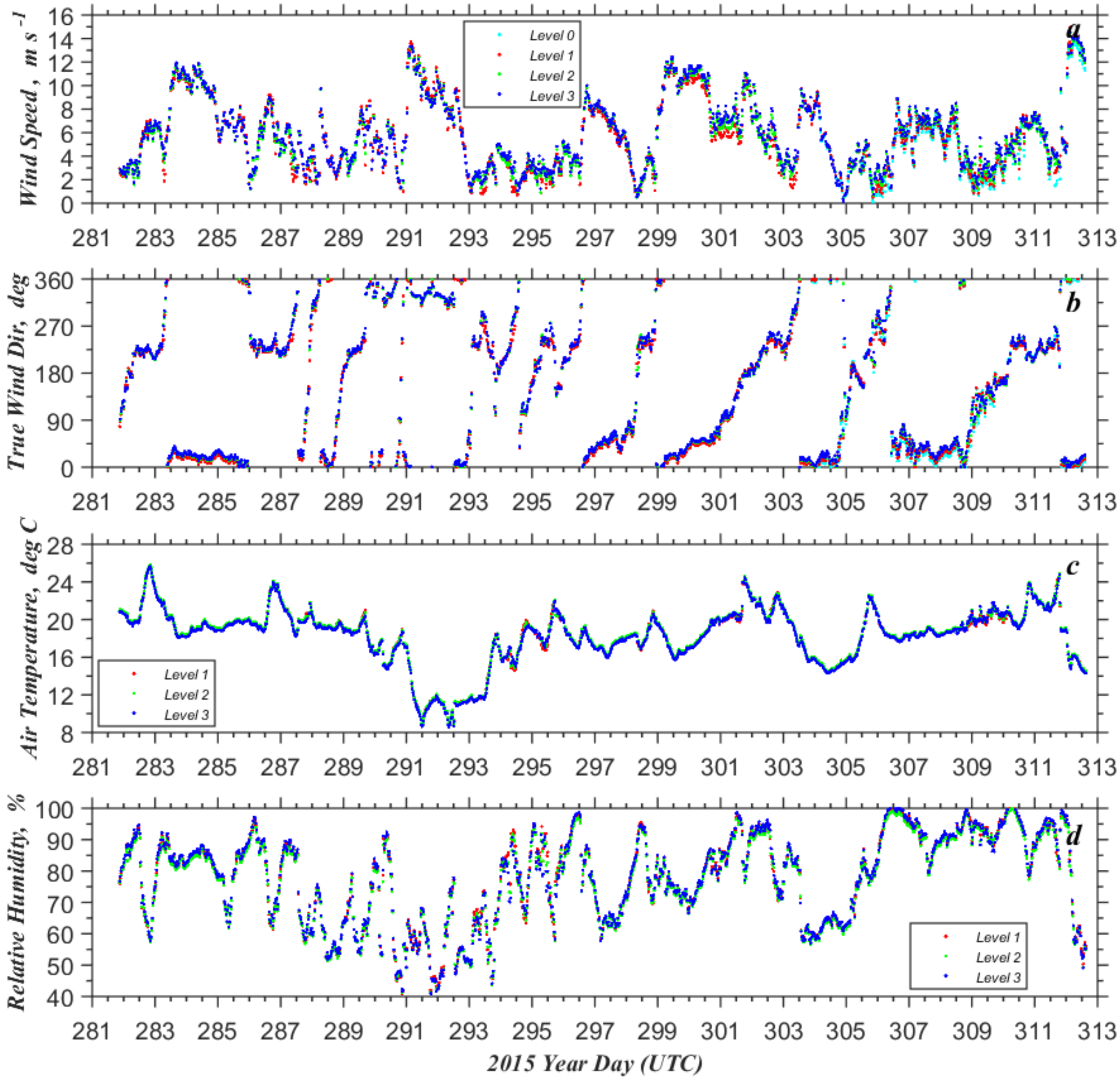

Fig 4 Time series of (*a*) wind speed, (*b*) true wind direction, (*c*) air temperature, and (*d*) relative humidity for the year days 281–313 (8 October–9 November 2015) observed over water at the Pier flux tower. The data are based on 30-min averaging.

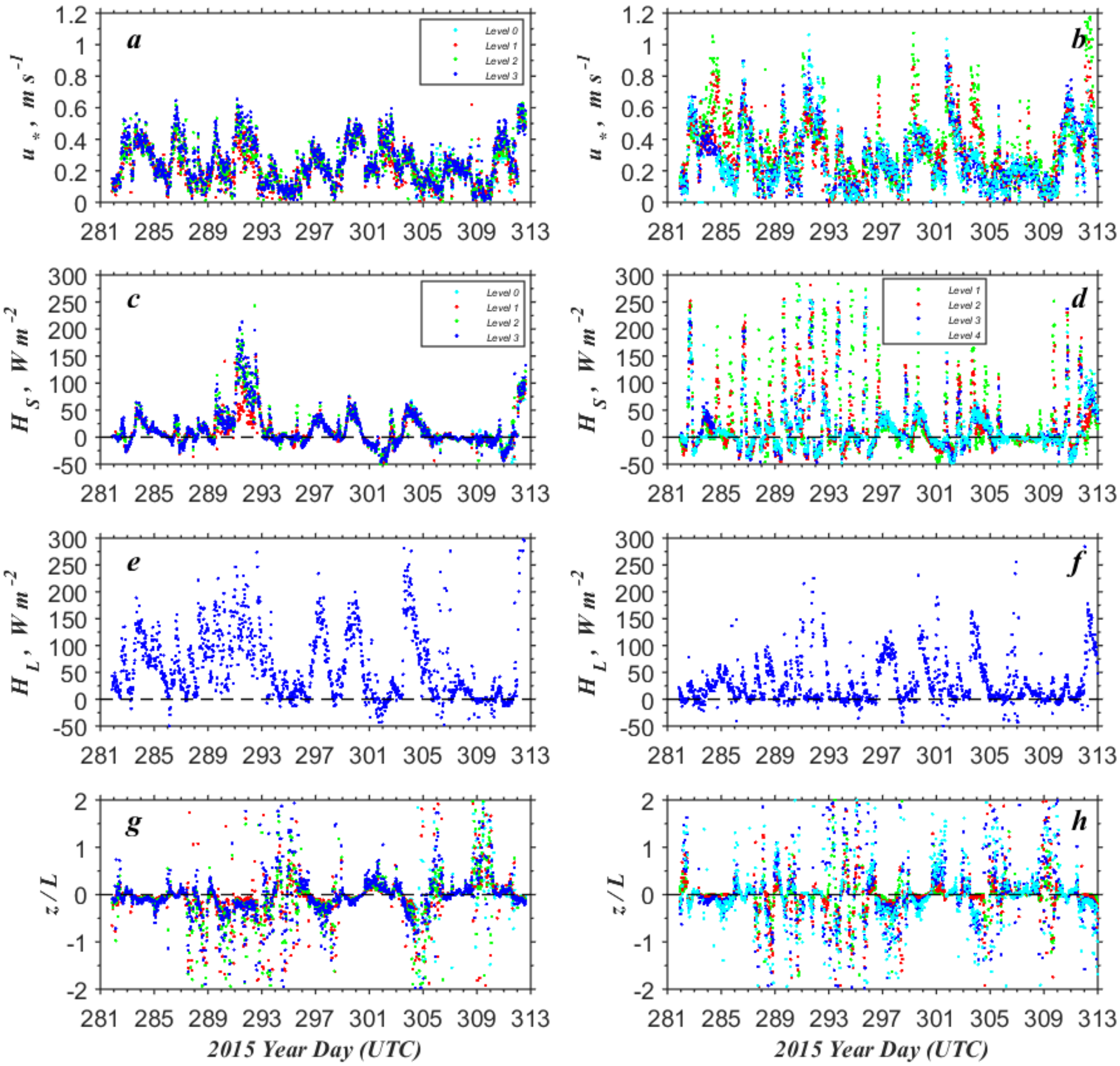

Fig 5 Time series of (*a*, *b*) friction velocity u_*, (*c*, *d*) sensible heat flux H_S, (*e*, *f*) latent heat flux H_L, and (*g*, *h*) Monin-Obukhov stability parameter $\zeta = z/L$ for year days 281–313 (8 October–9 November 2015) observed over water at the FRF Pier tower (panels *a*, *c*, *e*, and *g*) and over land at the FRF Video tower (panels *b*, *d*, and *h*) and the SDT flux tower (panel *f*). The data are based on 30-min averaging. The sign convention for the sensible heat flux generally indicates a stable boundary layer (SBL) when H_S < 0 and a convective boundary layer (CBL) when H_S > 0.

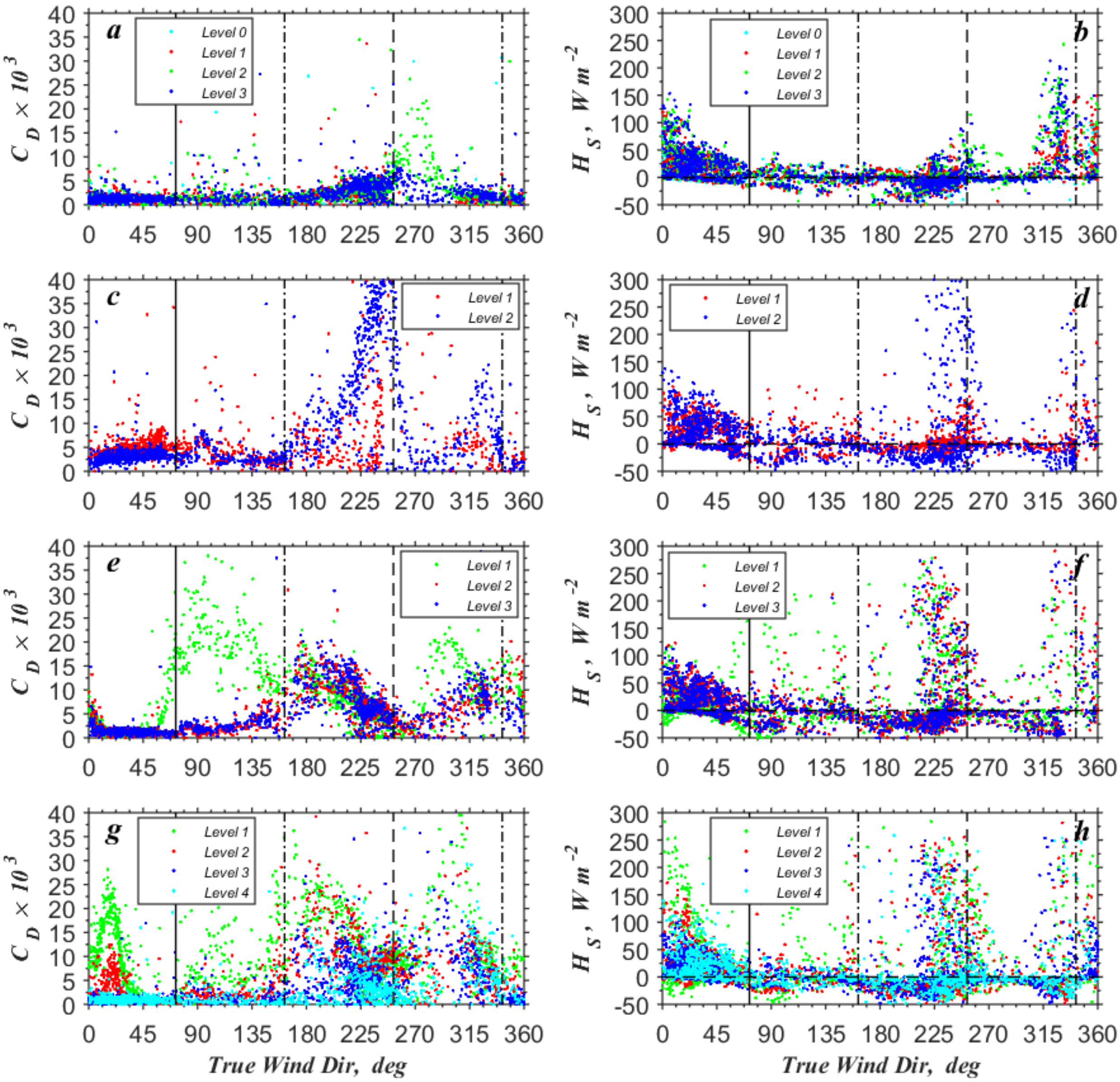

Fig 6 Drag coefficient $C_D = (u_* / U)^2$ (left panels *a*, *c*, *e*, *g*) and sensible heat flux H_S (right panels *b*, *d*, *f*, *h*) based on 30-min averaged data plotted versus the true wind direction for data collected at the (*a*, *b*) Pier, (*c*, *d*) SDF, (*e*, *f*) SDT, and (*g*, *h*) Video towers during 8 October–9 November 2015 (DOY 281–313). The pier is oriented ≈72° from north (solid vertical line), perpendicular to the shoreline. Onshore wind directions range from 342° through 162° clockwise (dash-dot vertical lines). The vertical dashed line indicates a direction opposite to the pier orientation (bearing ≈252°).

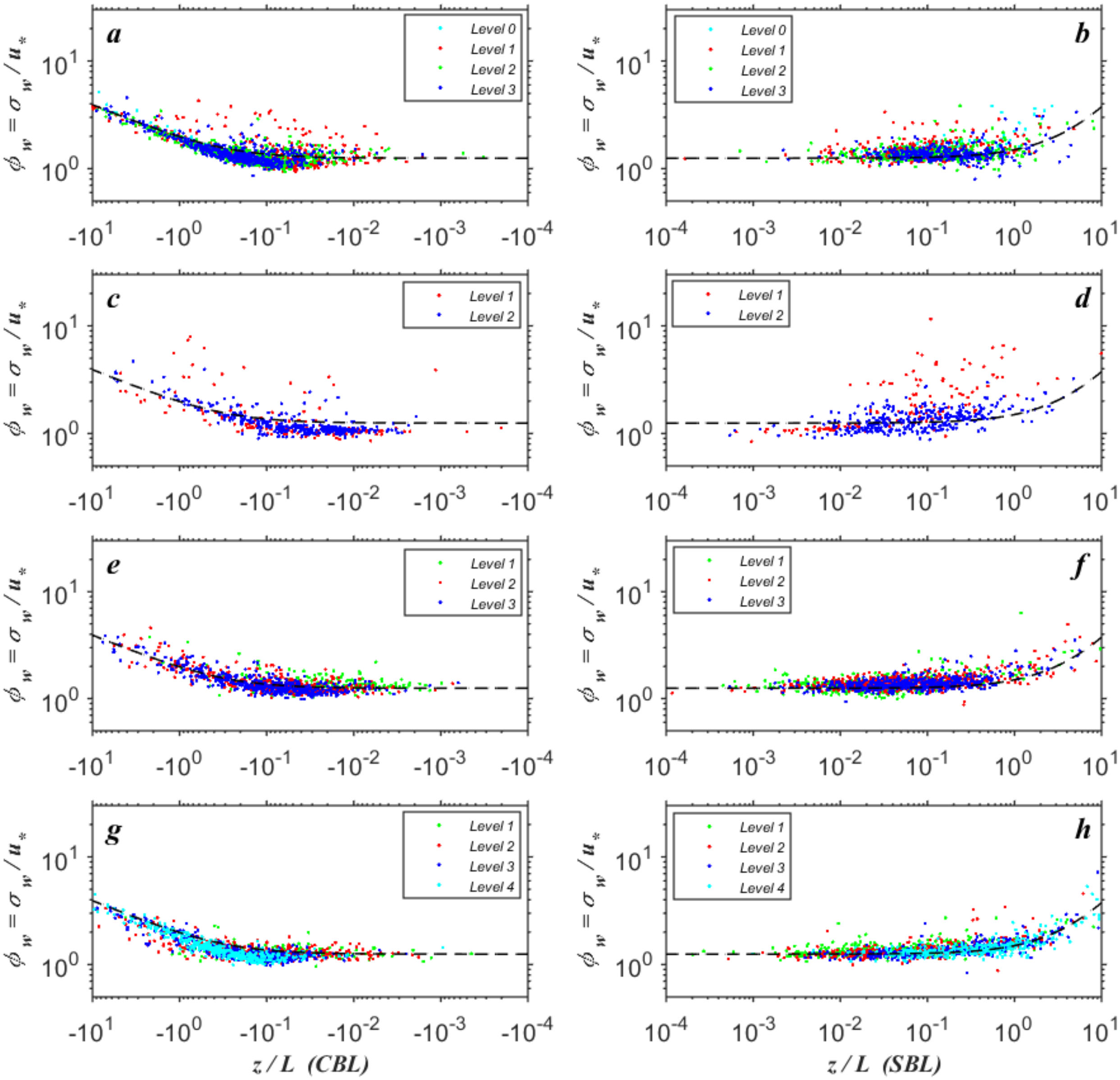

Fig 7 The non-dimensional standard deviation of the vertical velocity component $\varphi_w = \sigma_w / u_*$ (Eq. 7a), plotted in logarithmic coordinates versus the local Monin-Obukhov stability parameter $\zeta = z / L$ for the 30-min-averaged data collected at the (*a*, *b*) Pier, (*c*, *d*) SDF, (*e*, *f*) SDT, and (*g*, *h*) Video towers during 8 October–9 November, 2015 (DOY 281–313). The left panels (*a*, *c*, *e*, *g*) correspond to unstable conditions, or the convective boundary layer (CBL), $\zeta < 0$; the right panels (*b*, *d*, *f*, *h*) represent stable conditions, or the stable boundary layer (SBL), $\zeta > 0$. The dashed lines correspond to $\varphi_w = 1.25(1-3\zeta)^{1/3}$ for $\zeta < 0$ and $\varphi_w = 1.25(1+0.2\zeta)$ for $\zeta > 0$ (Kaimal and Finnigan 1994, Eq. 1.33).

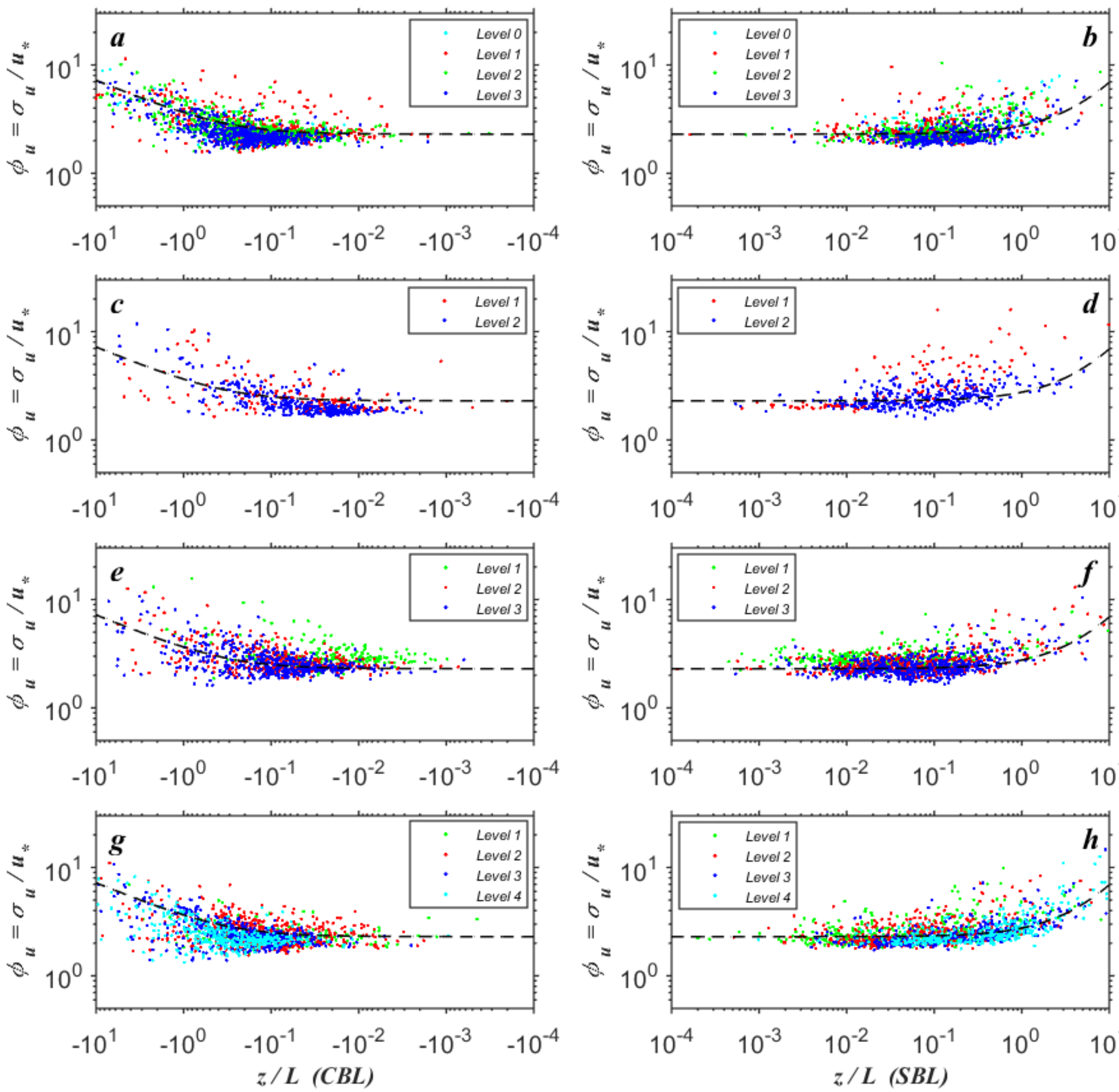

Fig 8 As for Fig. 7, but for the normalized standard deviation of the longitudinal velocity component $\varphi_u = \sigma_u / u_*$, Eq. 7a. The dashed lines represent $\varphi_u = 2.3(1-3\zeta)^{1/3}$ for $\zeta < 0$ (*a*, *c*, *e*, *g*) and $\varphi_u = 2.3(1+0.2\zeta)$ for $\zeta > 0$ (*b*, *d*, *f*, *h*) (Kaimal and Finnigan 1994, Eq. 1.33).

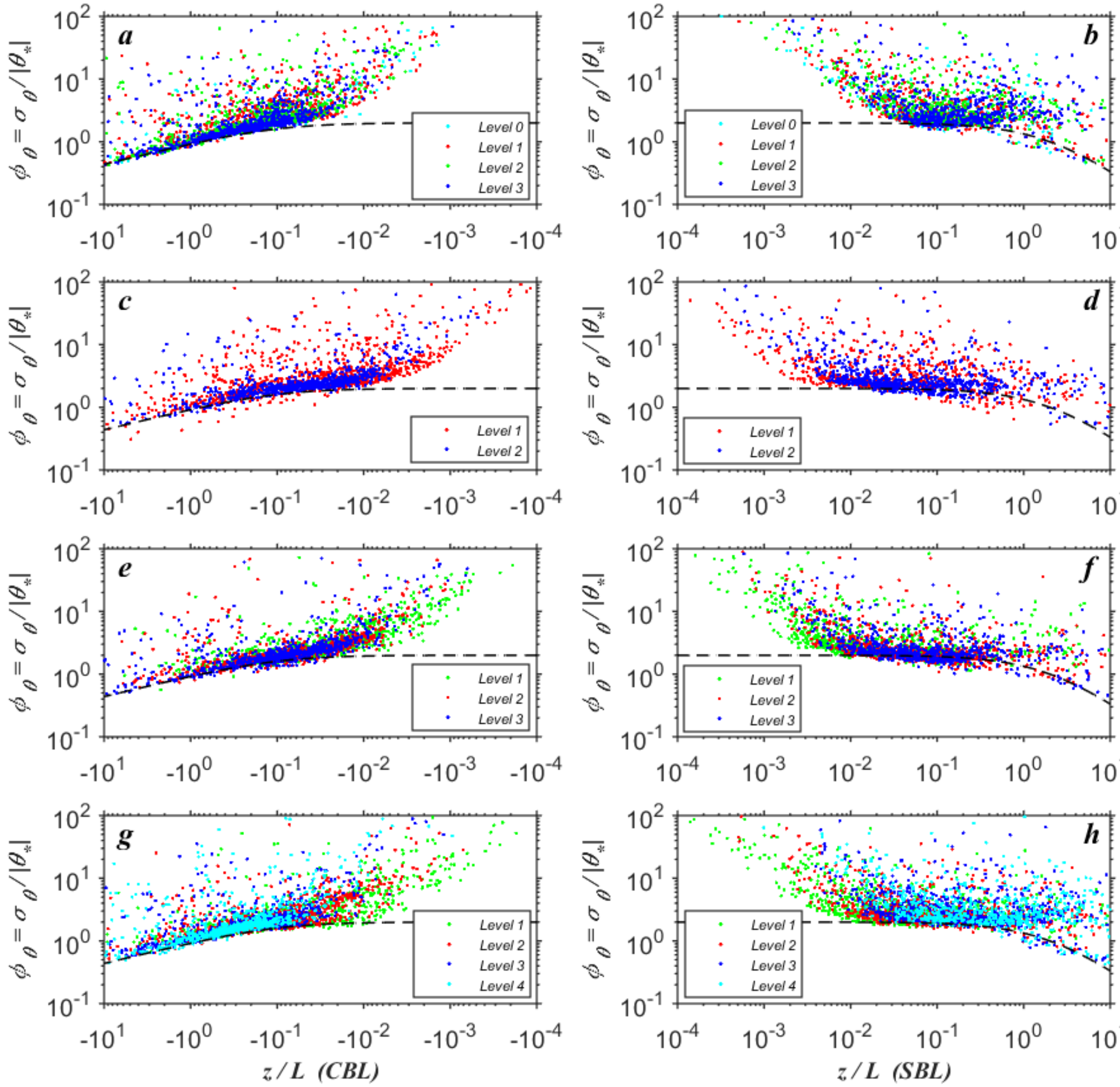

Fig 9 As for Fig. 7, but for the normalized standard deviation of the sonic temperature $\varphi_\theta = \sigma_\theta / |\theta_*|$, Eq. 7b. The dashed lines correspond to $\varphi_\theta = 2(1-9.5\zeta)^{-1/3}$ for $\zeta < 0$ (*a*, *c*, *e*, *g*) and $\varphi_\theta = 2(1+0.5\zeta)^{-1}$ for $\zeta > 0$ (*b*, *d*, *f*, *h*) (Kaimal and Finnigan 1994, Eq. 1.34).

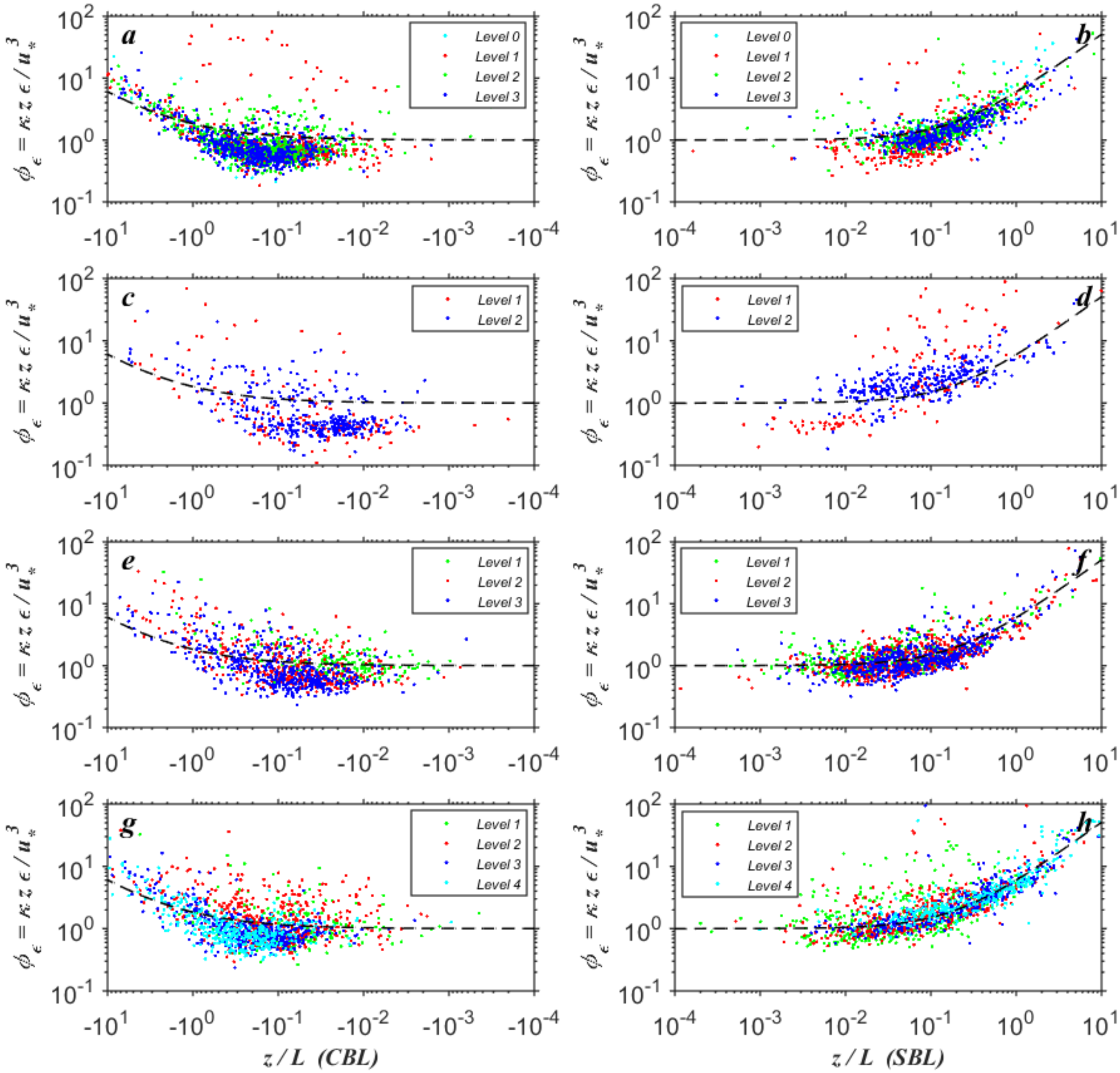

Fig 10 As for Fig. 7, but for the normalized dissipation rate of TKE $\varphi_\varepsilon = \kappa z \varepsilon / u_*^3$, Eq. 8, where ε is estimated based on a common method for measuring ε in a turbulent flow that assumes the existence of an inertial subrange associated with a Richardson-Kolmogorov cascade. Data causing the spectral slope in the inertial subrange to deviate by more than 20% of the theoretical –5/3 slope are excluded from the analysis. The dashed lines correspond to $\varphi_\varepsilon = (1 + 0.5|\zeta|^{2/3})^{3/2}$ for $\zeta < 0$ (*a*, *c*, *e*, *g*) and $\varphi_\varepsilon = 1 + 5\zeta$ for $\zeta > 0$ (*b*, *d*, *f*, *h*) (Kaimal and Finnigan 1994, Eq. 1.35).

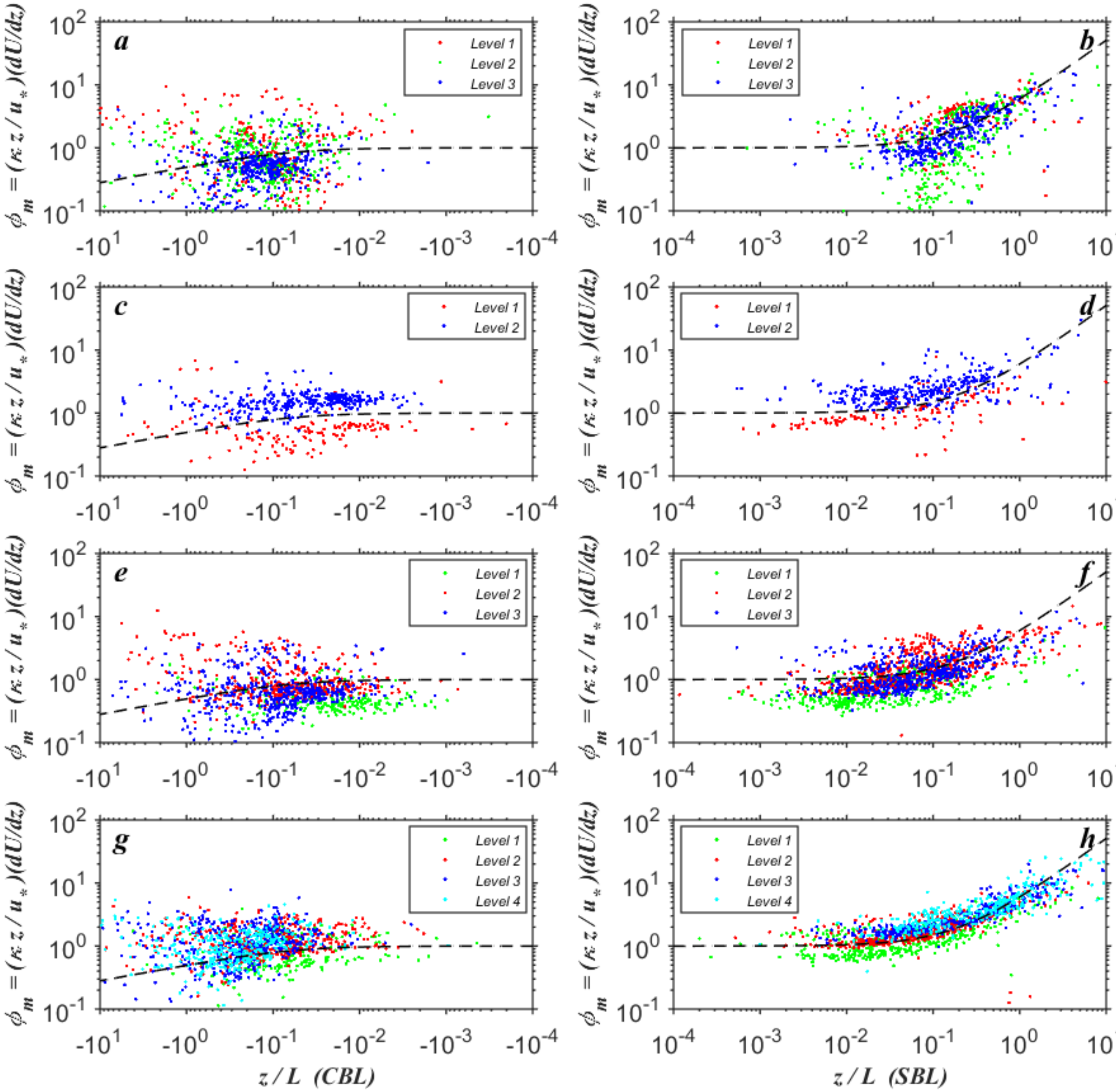

Fig 11 As for Fig. 7, but for the non-dimensional vertical gradient of mean wind speed $\varphi_m = (\kappa z / u_*)(dU / dz)$, Eq. 6a. The dashed lines correspond to the Businger–Dyer relationships $\varphi_m = (1 - 16\zeta)^{-1/4}$ for $\zeta < 0$ (*a*, *c*, *e*, *g*) and $\varphi_m = 1 + 5\zeta$ for $\zeta > 0$ (*b*, *d*, *f*, *h*) (Kaimal and Finnigan 1994, Eq. 1.31).

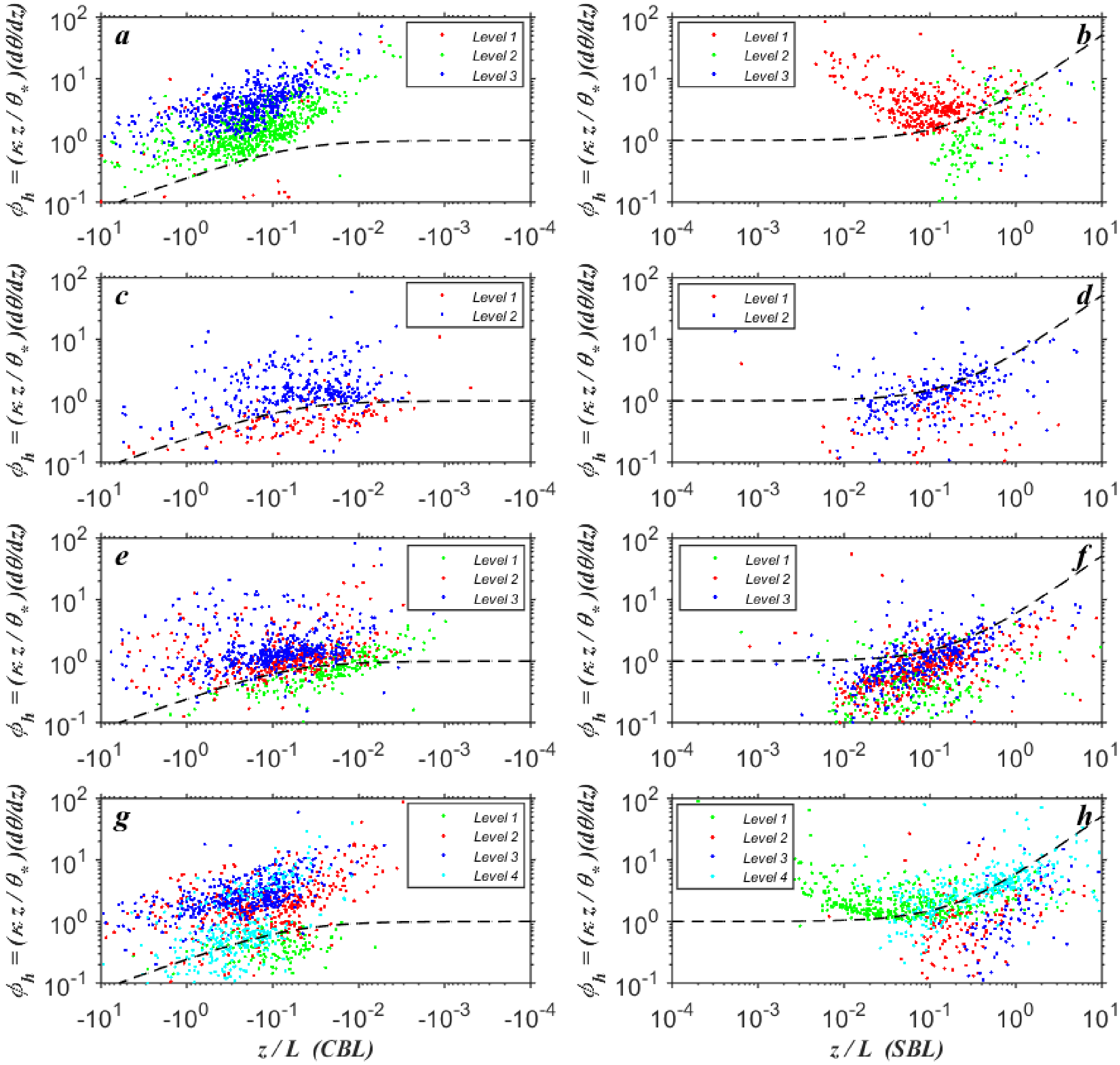

Fig 12 As for Fig. 7, but for the non-dimensional vertical gradient of mean potential temperature $\varphi_h = (\kappa z / \theta_*)(d\theta / dz)$, Eq. 6b. The dashed lines correspond to Businger–Dyer relationships $\varphi_h = (1-16\zeta)^{-1/2}$ for $\zeta < 0$ (*a*, *c*, *e*, *g*) and $\varphi_h = 1+5\zeta$ for $\zeta > 0$ (*b*, *d*, *f*, *h*) (Kaimal and Finnigan 1994, Eq. 1.32).

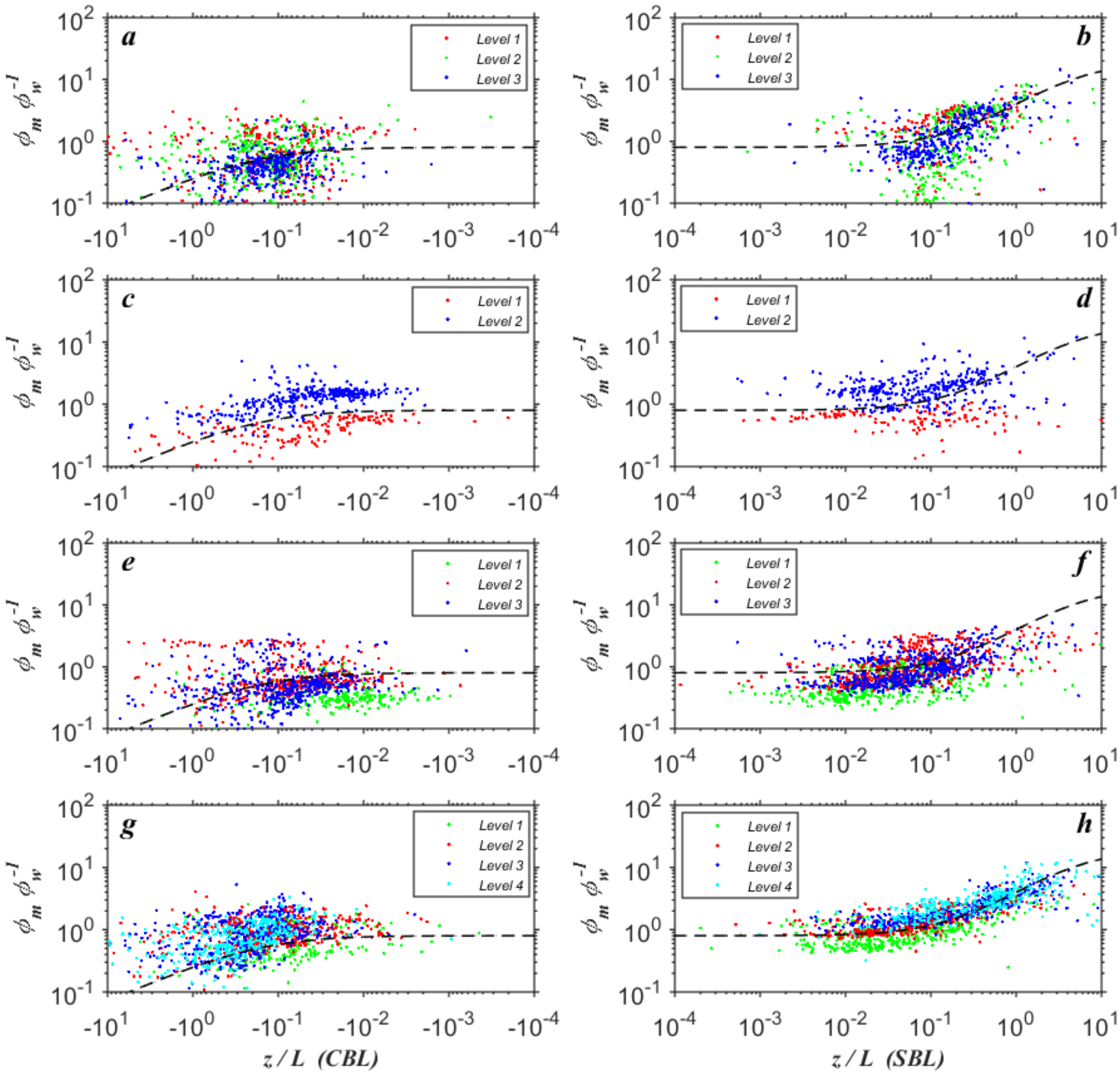

Fig 13 As for Fig. 11, but for the function $\varphi_m \varphi_w^{-1} = \left(\dfrac{\kappa z}{\sigma_w}\right)\dfrac{dU}{dz}$, which is a combination of the universal functions (6a) and (7a) for $\alpha = w$, and is not affected by self-correlation. The dashed lines correspond to $\varphi_m \varphi_w^{-1} = 0.8(1-16\zeta)^{-1/4}(1-3\zeta)^{-1/3}$ for $\zeta < 0$ (*a*, *c*, *e*, *g*) and $\varphi_m \varphi_w^{-1} = 0.8(1+5\zeta)(1+0.2\zeta)^{-1}$ for $\zeta > 0$ (*b*, *d*, *f*, *h*) (Kaimal and Finnigan 1994, Eqs. 1.31 and 1.33).

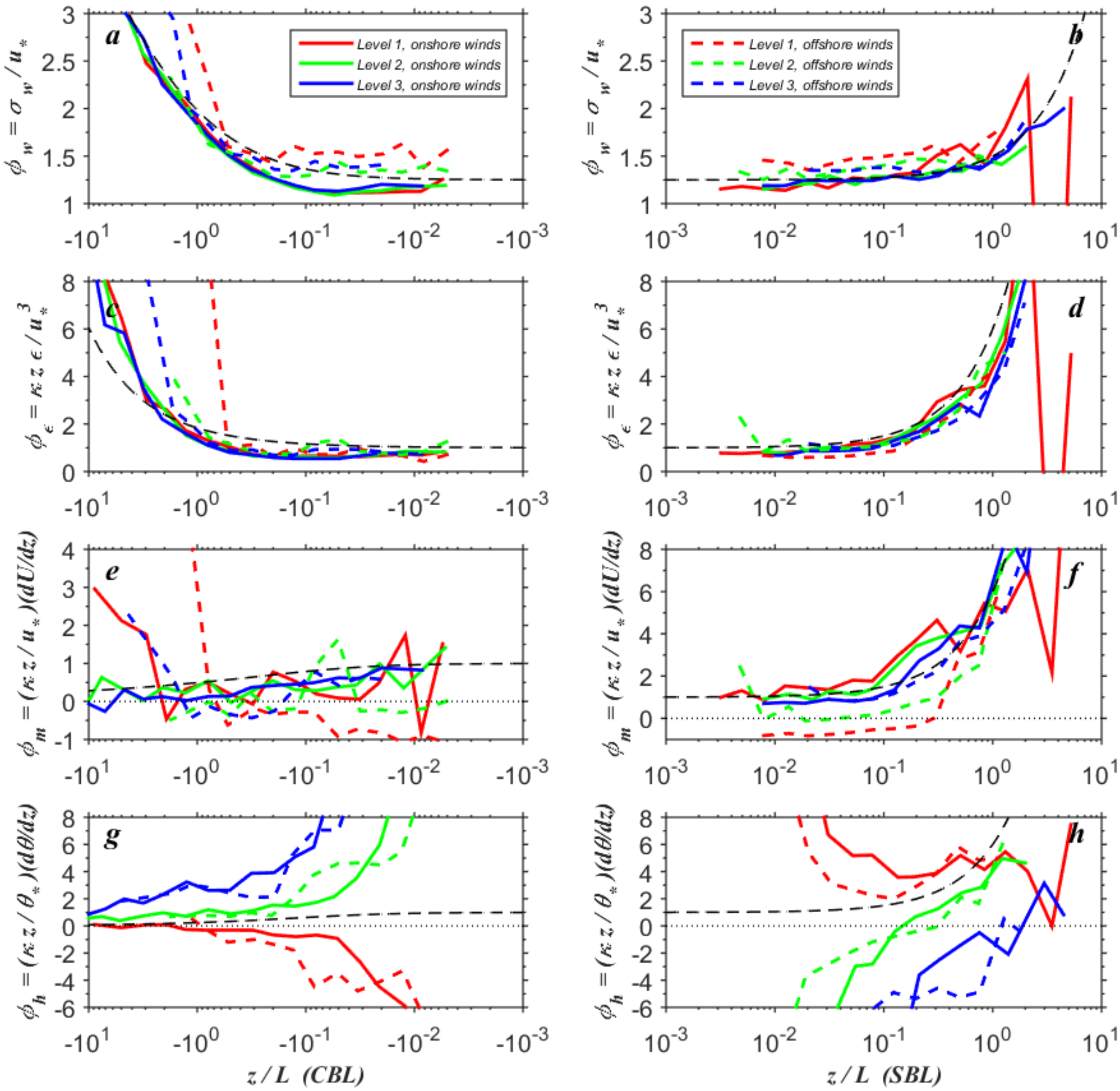

Fig 14 Plots of the bin-averaged non-dimensional universal functions (*a*, *b*) φ_w, (*c*, *d*) φ_ε, (*e*, *f*) φ_m, and (*g*, *h*) φ_h in logarithmic-linear coordinates versus the local Monin-Obukhov stability parameter $\zeta = z / L$ for the data collected over water at the Pier tower during 8 October–9 November, 2015 (DOY 281–313). The left panels (*a*, *c*, *e*, *g*) represent unstable conditions, or the convective boundary layer (CBL), $\zeta < 0$; the right panels (*b*, *d*, *f*, *h*) represent stable conditions, or the stable boundary layer (SBL), $\zeta > 0$. The coloured solid and dashed lines correspond to onshore and offshore flow, respectively. The black dashed lines are the Kansas-type relationships reported by Kaimal and Finnigan (1994, Eqs. 1.31–1.33, 1.35).

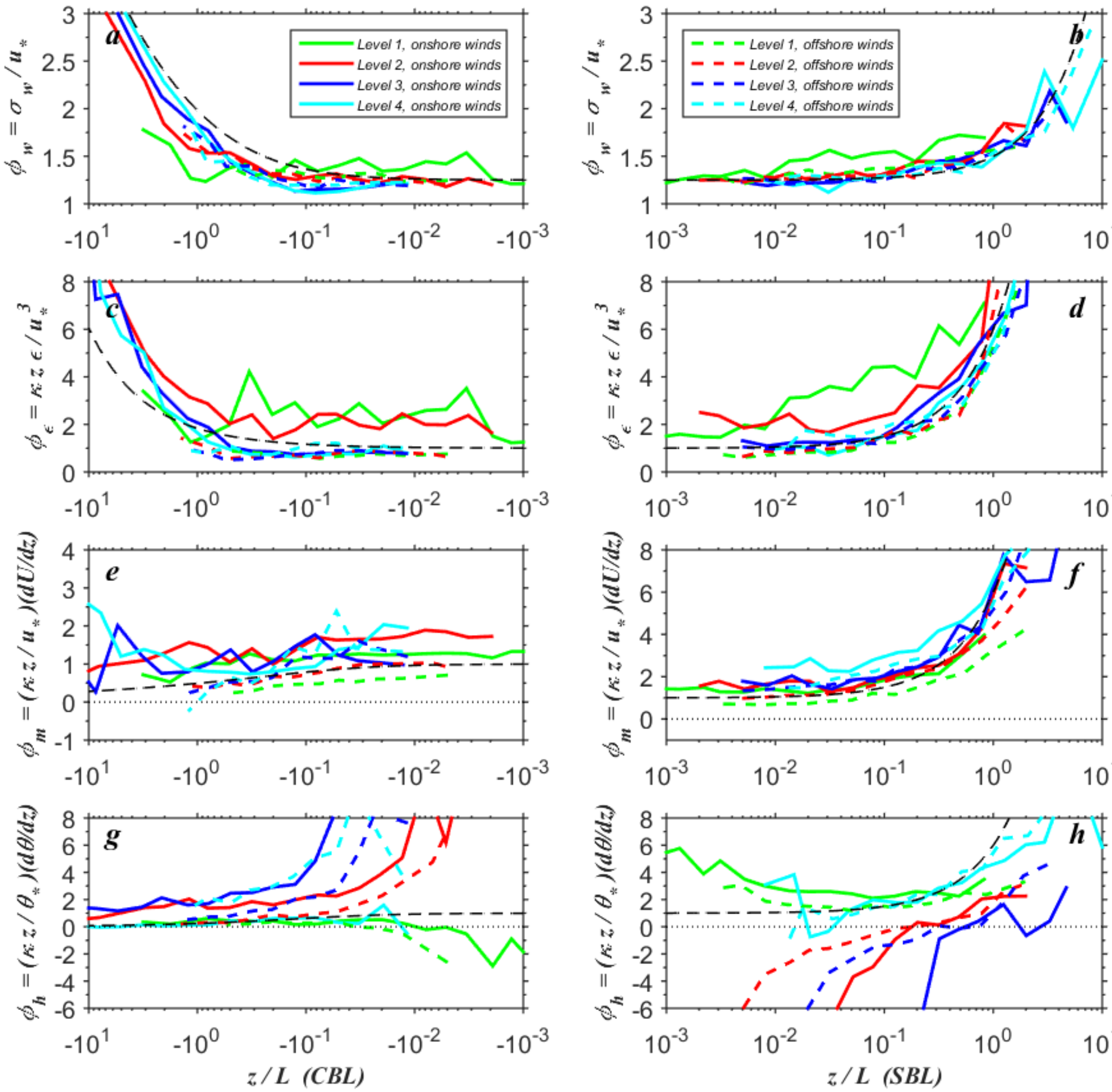

Fig 15 As for Fig. 14, but for the non-dimensional universal functions observed over land at the Video tower.